Remote Sensing of Environment 275 (2022) 113003

Contents lists available at ScienceDirect

Remote Sensing of Environment

journal homepage: www.elsevier.com/locate/rse

Annual forest disturbance intensity mapped using Landsat time series and field inventory data for the conterminous United States (1986–2015)

Jiaming Lu [a,*], Chengquan Huang [a], Xin Tao [b], Weishu Gong [a], Karen Schleeweis [c]

[a] Department of Geographical Sciences, University of Maryland, College Park, USA
[b] Department of Geography, University at Buffalo, the State University of New York, Buffalo, NY 14261, USA
[c] USDA Forest Service, Rocky Mountain Research Station, Ogden, UT 84401, USA

ARTICLE INFO

Keywords:
Disturbance intensity
Forest
Landsat
FIA

ABSTRACT

Forest disturbances can have broad impact on the climate, local environment, and the regeneration of the forest ecosystem. The nature and magnitude of such impact is largely driven by disturbance intensity. In this study, by integrating field plot measurements collected by the Forest Inventory and Analysis program with time series Landsat observations, we produced the first set of annual forest disturbance intensity map products quantifying the percentage of basal area removal (PBAR) at the 30-m resolution for the conterminous United States (CONUS) from 1986 to 2015. The derived map products revealed that during the 30-year study period, the annual average PBAR values of all disturbed pixels across CONUS ranged from 66% to 70%, and the proportion of those pixels having stand-clearing disturbances ranged from 40% to 58%. High disturbance intensities were concentrated in the Southeastern states from Texas to Virginia and along the Pacific coast and the Cascades in the West. At the national scale, the annual mean PBAR and proportion of stand clearing area (PSCA) values both appeared to follow second order trajectories, with increasing trends at the beginning, decreasing trends towards the end, and turning points around 2003. Overall, there is a net increase of 2% in PBAR and 3% in PSCA from 1986 to 2015. The temporal trends of PBAR and PSCA were also investigated at state and ecoregion levels, with substantial differences found among many states and ecoregions. While states and ecoregions generally follow second order trajectories, the majority had increasing trends throughout much of the study period, reflecting higher disturbance intensities during the later years compared to earlier years. Large increase (>10%) in PBAR was seen in several states (e.g., Virginia, Arkansas, and Minnesota) and ecoregions (e.g., Northern Minnesota Wetlands); however, large decreases (>10%) in PBAR were not observed in any states, and were seen in only one ecoregion, the Blue Mountains in the southeast. The disturbance intensity maps are available from a web portal of the Oak Ridge National Laboratory Distributed Active Archive Center (ORNL-DAAC) at https://doi.org/10.3334/ORNLDAAC/2059.

1. Introduction

Forests are shaped by many processes, including both disturbance history and post-disturbance succession. Recently, anthropogenic and natural disturbances have changed the forests on Earth on an unprecedented scale (Pickett and White, 2013; Turner et al., 1993). During the last 300 years, human activities, including timber removals and deforestation for agricultural use, have been estimated to affect over 50% of global land surface and permanently cleared over 25% of forests (Hurtt et al., 2011; Vitousek et al., 1997). Natural disturbances (e.g., wind, fire, insects, hurricane and disease), as part of the natural forest development cycle, also modify forest compositions and affect the cycle of regeneration and regrowth (Chambers et al., 2007; Seidl et al., 2017; Sieg et al., 2017). Disturbance-induced forest changes have consequently affected climate, biodiversity and other ecosystem services provided by forests (Thom and Seidl, 2016).

Since the 1970s, Landsat has been providing multi-decades observations over the Earth's surface (Cohen and Goward, 2004). The opening of the Landsat archive for free access in 2008 (Woodcock et al., 2008) marked a new era for utilizing Earth observation data to document changes to terrestrial ecosystems at large space scales, including developing novel methods in forest disturbance mapping (Hansen and

* Corresponding author at: Department of Geographical Sciences, University of Maryland, College Park, USA.
E-mail address: jmlu@terpmail.umd.edu (J. Lu).

https://doi.org/10.1016/j.rse.2022.113003
Received 20 August 2021; Received in revised form 10 March 2022; Accepted 13 March 2022

Loveland, 2012). Many algorithms have been developed to estimate the occurrence location, extent, time and duration of disturbances by detecting changes in spectral trajectory from Landsat time series (DeVries et al., 2015; He et al., 2011; Hermosilla et al., 2015; Huang et al., 2010a; Kennedy et al., 2010; White et al., 2017; Zhu et al., 2019b). Forest disturbance products have been produced at national to global scales (Hansen et al., 2013; White et al., 2017; Zhao et al., 2018).

Given these rapid developments, however, much less progress has been made in quantifying a key aspect of forest disturbance using remote sensing data – disturbance intensity. Disturbance intensity immediately affects the changes of forest structure, composition (Panfil and Gullison, 1998; Parrotta et al., 2002), subsequent forest productions (Egnell, 2017), and plant litter input. The changes caused by disturbances, dictated by their intensities lead to long-term impacts on forest carbon storage (Scheller et al., 2011), soil carbon and nutrient stocks (Akselsson et al., 2007; Mushinski et al., 2017; Olsson et al., 1996; Yanai et al., 2003), and microbial communities in adjacent water environment (Reid et al., 2010). Knowing how disturbance intensity changes over time and how forests respond to historical disturbances will help in evaluating disturbance risk, preparing for future disturbances, and minimizing their negative effects (Buma and Schultz, 2020; Thom and Seidl, 2016).

Ground-based quantification of disturbance intensity requires field measurements made before and after a disturbance event. Such repeat measurements are mandated by the National Forest Inventories (NFIs) programs of increasingly more countries. The US Forest Service (USFS) Forest Inventory and Analysis (FIA) program is one of the oldest and largest NFI program (Bechtold and Patterson, 2005; Gelfand et al., 2013; McRoberts et al., 2005). While repeat FIA measurements allow for the estimation of attribute changes over time (Bechtold and Patterson, 2005; Fridman et al., 2014), the spatial distribution of FIA plot designs cannot always provide the spatial resolution necessary for all applications (McRoberts and Tomppo, 2007; Tomppo et al., 2008). Tracking annual forest disturbances with strategic national field inventories alone is challenging given the highly localized and clustered nature of many natural disturbance processes in space and time (Bradford et al., 2010). Further, tree regrowth rates after disturbance can be very rapid in areas with high productivity or management, confounding field data collected at 5-year or longer intervals. Image-based remote sensing can provide spatially contiguous and frequent observations useful to detect disturbance location, extent, and severity over large areas.

In previous studies, disturbance magnitude has been calculated as the difference of spectral reflectance ratio based indices between pre- and post-disturbance observations (Huang et al., 2010b; Kennedy et al., 2010). While the calculated disturbance magnitude can be used as the approximation to the disturbance severity or intensity (Huang et al., 2015; Ling et al., 2016; Senf and Seidl, 2021), this spectral change cannot be directly used to measure the biophysical consequences of a disturbance event. The quantification of a disturbance's impact on biophysical variables such as changes in biomass, basal area, and height would require accurate reference data from pre- and post-disturbance events. Following the concept that harvest intensity can be estimated as changes in basal area and canopy cover (Healey et al., 2006; Hill et al., 2015), Tao et al. (2019) demonstrated the feasibility of combining Landsat time series and multi-temporal field measurements to quantify disturbance intensity in North and South Carolina for over 30 years. Here disturbance intensity, measured by changes in basal area, is a combination of both natural disturbance severity and anthropogenic activity intensity (e.g., logging intensity). Building on that study, the objective of this research was to test the applicability of the approach over larger geographies, then use it to generate yearly maps of forest disturbance intensity in the conterminous United States (CONUS) from 1986 to 2015. The resultant maps provided spatially explicit quantitative estimates of changes in basal area following each disturbance event. We examined the spatial patterns and temporal trends of disturbance intensity across CONUS at both the state and the level-3 ecoregion level (U.S. Environmental Protection Agency, 2010). The derived map products will not only provide a more precise quantification of forest disturbances across the US, but they can also be used to derive a more accurate assessment of the impacts of those disturbances on ecological functions.

2. Methodology

2.1. Data

2.1.1. Landsat time series stacks

Landsat time series stacks (LTSS) (Huang et al., 2009) were used to detect disturbance occurrence in this study. LTSS were formed by ready-to-use Landsat 5 TM, Landsat 7 ETM+ and Landsat 8 OLI images that were acquired from leaf-on season with minimum cloud cover (<5%) and shadows, which had been geometrically and radiometrically corrected using the Landsat Ecosystem Disturbance Adaptive Processing System (LEDAPS) to produce surface reflectance data (Huang et al., 2009; Masek et al., 2006). The cloud fraction of each Landsat image was calculated based on a cloud and shadow mask generated using a cloud masking algorithm developed by Huang et al. (2010b). If multiple images with less than 5% cloud cover were available, the image with least cloud cover was selected. If there are multiple images with similarly low cloud cover, we selected the image acquired on the Julian day of year (DOY) nearest to the center of the DOY range for this Worldwide Reference System-2 (WRS2) scene. When no cloud-free image could be found for a specific year, multiple partially cloudy (<50%) images from that leaf-on season were used to create an image composite that had less than 5% cloud cover (Zhao et al., 2018). The compositing algorithm first selected the image having the most clear-view pixels as the composite base image. If a pixel in the base image was not acceptable due to cloud/shadow or other data quality issues, a clear-view observation at that pixel location was selected from other available images based on a maximum normalized temperature compositing rule, which was then used to replace the pixel in the base image (Zhao et al., 2018). More details on the image selection and compositing methods have been provided by Schleeweis et al. (2016) and Zhao et al. (2018).

A total of 434 WRS2 scenes were required to provide a near complete coverage of CONUS. An annual LTSS was constructed for each scene, which comprised of about 30 cloud-free or near cloud-free images – one per year for the years from 1986 to 2015.

2.1.2. FIA plot data

Reference disturbance intensity data was derived from the FIA database. FIA has over 377,000 plots, with roughly 1/3 forest sample plots, distributed across the nation (Smith, 2002). Starting in 2000, FIA plots were divided into 5 panels in the eastern states (see northern region and southern region states in Table 1) and 10 panels in the western states (see interior west region and Pacific northwest region states in Table 1) with the intention to measure one panel per year (Gillespie, 1999). The panel design samples 14–20% of eastern plots and 10% of western plots each year with the full state remeasured inventories completed roughly every 5 years for eastern states and 10 years for western states. A panel corresponds to a measurement year of the 5-year or 10-year cycle. After the last panel is measured, the cycle is repeated. For example, for most eastern states, if the plots from panel 1 were measured in 2010, each of the remaining four panels (2–5) would be assigned to the four succeeding years (2011–2014) and plots from panel 1 will be measured again in 2015 (Brand et al., 2000). Additionally, each panel's design ensures a statistically balanced sample of plots that can estimate forest inventory variables annually for the entire state. During each field visit, the FIA crew measures the diameter at breast height (d.b.h) for timber species, the diameter at the stem root collar (d.r.c) for woodland species. Trees ≥12.7 cm d.b.h./d.r.c located within subplots and trees <12.7 cm d.b.h./d.r.c located within microplots are measured for other attributes. See FIA Field Guide (2019) for explanation of variables and the plot design. Repeat measurements at the same plot on

Table 1
Distributions and year range of FIA plots used in this study by state and FIA regions.

FIA Region	State	Abbreviations	Plot Counts	Area (km^2)	Measurement Year Range
Southern Region (2575 plots)	Alabama	AL	326	135,765	1999–2017
	Arkansas	AR	253	137,732	1999–2017
	Florida	FL	120	170,312	2001–2016
	Georgia	GA	319	153,910	1999–2017
	Kentucky	KY	41	104,656	1999–2017
	Louisiana	LA	212	135,659	2000–2017
	Mississippi	MS	171	125,438	2006–2017
	North Carolina	NC	246	139,391	1999–2017
	Oklahoma	OK	34	181,037	2007–2015
	South Carolina	SC	293	82,933	1999–2016
	Tennessee	TN	98	109,153	1999–2017
	Texas	TX	232	695,662	2002–2017
	Virginia	VA	230	110,787	1999–2017
Northern Region (483 plots)	Connecticut	CT	1	14,357	2009–2015
	Delaware	DE	4	6446	2007–2017
	Illinois	IL	2	149,995	2008–2017
	Indiana	IN	5	94,326	2002–2016
	Iowa	IA	1	145,746	2007–2012
	Kansas	KS	1	213,100	2004–2009
	Maine	ME	102	91,633	2001–2017
	Maryland	MD	4	32,131	2006–2013
	Massachusetts	MA	1	27,336	2011–2015
	Michigan	MI	88	250,487	2001–2017
	Minnesota	MN	122	225,163	2000–2017
	Missouri	MO	57	180,540	2002–2017
	Nebraska	NE	2	200,330	2008–2016
	New Hampshire	NH	7	24,214	2004–2016
	New Jersey	NJ	1	22,591	2005–2009
	New York	NY	8	141,297	2003–2017
	North Dakota	ND	0	183,108	N/A
	Ohio	OH	21	116,098	2002–2017
	Pennsylvania	PA	26	119,280	2002–2017
	Rhode Island	RI	0	4001	N/A
	South Dakota	SD	22	199,729	2001–2017
	Vermont	VT	2	24,906	2008–2016
	Wisconsin	WI	0	169,635	N/A
	West Virginia	WV	6	62,756	2004–2014
Interior West Region (220 plots)	Arizona	AZ	31	295,234	2001–2017
	Colorado	CO	9	269,601	2003–2016
	Idaho	ID	72	216,443	2004–2017
	Montana	MT	89	380,831	2003–2017
	New Mexico	NM	11	314,917	2010–2017
	Nevada	NV	1	286,380	2004–2014
	Utah	UT	7	219,882	2000–2017
	Wyoming	WY	0	253,335	N/A
Pacific Northwest Region (276 plots)	California	CA	61	423,967	2001–2017
	Oregon	OR	129	254,799	2001–2017
	Washington	WA	86	184,661	2002–2016

different dates can be used to calculate changes in volume or basal area resulting from disturbances that occurred between those two dates

Not all FIA plots were used to calculate reference disturbance intensity. Several criteria were applied to identify plots to be used as reference for this study. First, we excluded plots established in the periodic FIA phase prior to 1998, to ensure plot data was collected with the national standardized plot design and data collection procedures. Second, a plot was used if it had experienced disturbance between two consecutive annual inventories. This was determined by collocating exact locations of FIA plots with the 30 m VCT annual disturbance products. This ensures the measurements of sample trees pre- and post-disturbance are available for estimating the change. Third, a plot was used if it was not located on a forest patch edge, for the following reasons: (1) if a plot is located across disturbed patch edges, impact of disturbance on the trees within and outside the patch will be distinct, which can lead to underestimation of plot disturbance intensity (Tao et al., 2019); (2) when plots are linked to pixels, geolocation mismatch could introduce large uncertainties, given the up to ±30-m positional accuracy of Landsat terrain-corrected Level 1 (L1T) images (Storey et al., 2014; Storey et al., 2016). If four subplots are highly heterogeneous, both forest attribute change and its corresponding spectral change should be different across subplots. Due to the offset of pixel location, the forest attribute change of a plot could be associated with deviated spectral characteristics. The mismatch has been demonstrated to have a strong impact on the prediction accuracy of forest attributes, such as biomass (Frazer et al., 2011) and forest area (McRoberts et al., 2010). The calculation of reference disturbance intensity will be described in section 2.2.3.

2.2. Method

2.2.1. Method overview

The mapping algorithm used in this study generally follows the approach developed by Tao et al. (2019), which was used to generate forest disturbance intensity maps for North and South Carolina. In this study, we tested the approach over seven states in the Southeast region and over four FIA regions (Table 1) before applying it to the entire conterminous US (CONUS). Below we provide a brief summary of this algorithm, as more details have been provided by Tao et al. (2019). Here we focus more on the handling of reference data across CONUS, the development of disturbance products for CONUS, evaluation of the mapping approach at different scales (state, regional, and national), and

assessment of the quality of the resultant CONUS-wide disturbance intensity products and the spatial-temporal patterns revealed by those products. The mapping approach consists of four steps (Fig. 1). The first was to determine the disturbance year and calculate change of spectral indices from Landsat time series. The second was to derive reference disturbance intensity from repeat measurements on field inventory plots. The reference data were then used to train the Random Forest algorithm (Breiman, 2001) to establish the relationship between the spectral changes and basal area change. The random forest algorithm has been widely used to extrapolate plot measurements of biophysical variables or classification schemes of training samples to large areas with remote sensing data (Belgiu and Drăguţ, 2016; Pal, 2005). Finally, the model was applied to Landsat images covering the entire CONUS to produce annual wall-to-wall maps. The following sections describe the details in each step.

2.2.2. Disturbance product and spectral change metrics from Landsat

Disturbance maps used in this study were derived from Landsat time series stacks (LTSS) (Huang et al., 2009) using the vegetation change tracker (VCT) algorithm (Huang et al., 2010b). These products show the location and year of disturbances mapped at the 30 m resolution. For each disturbance detected, 10 magnitude measures, including 5 delta variables and 5 normalized ratio variables (Table A1), were calculated using several spectral bands and indices to represent the spectral change of the pre- and post-disturbance events as described in Tao et al. (2019). The indices include NDVI, normalized burn ratio (NBR), normalized difference moisture index (NDMI), IFZ, and forest z-score (FZ) calculated using Landsat bands 4 (B4FZ) and 5 (B5FZ) (Huang et al., 2010b). These were calculated using Eqs. (A1-A6) and were used as predictor variables modeling disturbance intensity.

2.2.3. Reference disturbance intensity derivation

Reference disturbance intensity data was derived from repeat measurements at the same FIA plots on different dates. Given the 5- to 10-year intervals between FIA remeasurements, however, changes in total basal area between two dates cannot be attributed solely to disturbance events. Growth of surviving trees and new trees between the two dates also contributes to an increase in basal area of a plot. Therefore, a simple difference of total basal area between two measures would include the growth, often resulting in an underestimation of the basal area change caused by disturbance events (Fig. 2)

To eliminate the effect of tree growth, each tree record was tracked by its sequence number through time. Only trees recorded in the prior inventory and absent from the next inventory are assumed to be affected or removed by disturbances between the two inventories. The difference between basal areas of these trees were then used to calculate the percentage of basal area removal (PBAR) as a measure of disturbance intensity following Eq. (1):

$$PBAR = \frac{TBA_1 - BA_{21}}{TBA_1} \quad (1)$$

where TBA_1 is the total basal area of all live trees at the first time of inventory, and BA_{21} is the total basal area measured at the prior inventory of trees alive at both inventories (Fig. 2). Note that the diameter measured at the second inventory was not used in the calculation. If we replace BA_{21} with TBA_2, the total basal area of all live trees at the second time of inventory, which is larger than BA_{21} because it includes the growth of existing trees (trees a and b in Fig. 2) and new trees (trees e,f and g in Fig. 2), this will lead to an underestimation of PBAR. PBAR ranges from zero to one, with zero indicating no basal area removed, and one indicating 100% basal area removed by disturbance. Note in this study PBAR measures the loss of basal area from all possible causes, not differentiating disturbance types.

After the calculation of PBAR for each disturbed plot, the calculated value was evaluated by visually examining available Google Earth (GE) high-resolution imagery to eliminate potential discrepancies between this value and the GE imagery. Plots with large discrepancies (e.g. calculated PBAR is less than 20% the GE images revealed that a stand-clearing event had occurred and vice versa) were removed from the reference dataset. During this screening process, all security precautions were taken per the FIA agreement, including no exact coordinates were used to search for locations on imagery in GE.

After the screening process (discussed in section 2.1.2 and the previous paragraph), 3554 qualified plot records over CONUS were available for use, with 2575 in the south, 483 in the north, 220 in the Interior West, and 276 in the Pacific Northwest (Table 1). Seven states in the southeast (NC, SC, GA, TN, MS, AL, FL) contribute 1573 records (about 44%) to all reference plots. The high density of available reference plots in the region is due to both the frequent and intensive timber harvesting activities in this part of the country, and the frequency of FIA full panels in the east compared to the west. The measurement years of reference plots range from 1999 to 2017 and the coverage varies by state, depending on the beginning year of transition to the annual inventory system of each state. For all the plots that passed the screening, percentage of PBAR is calculated from pre- and post-disturbance plot measurements in the FIA database, to characterize the impact of disturbance on the forest's biophysical properties, thus providing reference data to disturbance intensity modeling (Healey et al., 2006; Tao et al., 2019).

2.2.4. Algorithm assessment and national mapping

The effectiveness of the disturbance mapping approach had been

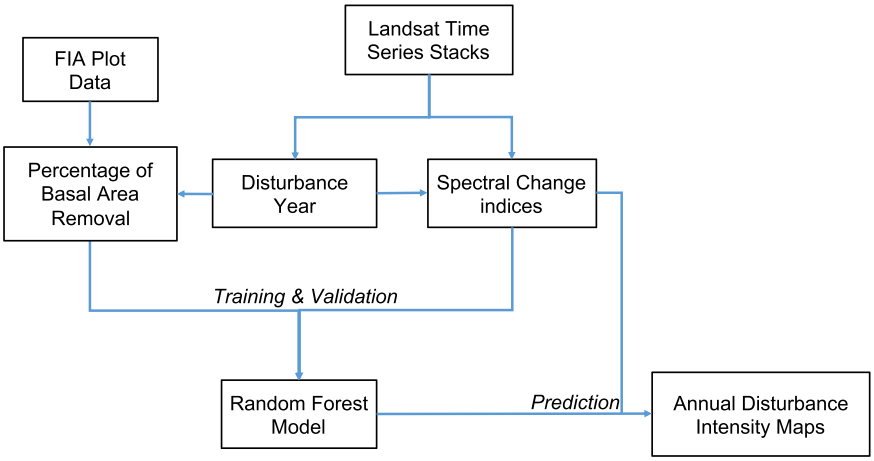

Fig. 1. Key steps of the disturbance intensity mapping framework.

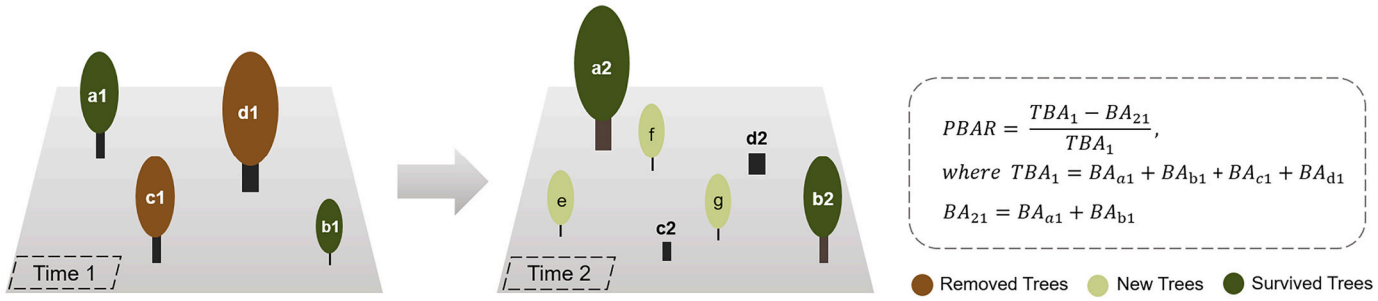

Fig. 2. An illustration of forest change between two inventory times showing basal area loss due to disturbance (trees c and d), gain from growth (trees a and b), and establishment of new trees (trees e, f, and g). In tree labels, the letter denotes which tree it is, and the number denotes the time of inventory (e.g., a1 means tree a measured at time 1). The basal area change caused by the disturbance event would be underestimated by a simple difference between the two inventories. Instead, it should be calculated using the equation Eq. (1).

previously demonstrated in only two states (Tao et al., 2019). To evaluate its robustness more comprehensively, we first tested it in each of the seven southeastern states (NC, SC, GA, TN, MS, AL, and FL). We then tested this approach with a model for each of the FIA regions (Table 1) as well as a single model for the entire CONUS. Our goal was to demonstrate the feasibility of using a single model to map disturbance intensity across CONUS to avoid issues that could arise from using multiple models: 1) some states or regions did not have enough reference plots for model development (Table 1), and 2) discontinuities could exist between adjacent states or regions if they were mapped using different models.

To evaluate the model for each geographic area, 10-fold cross validations were performed which randomly partitioned the reference plot samples into 10 subsets. Ten different models were built, each trained with 9 of the 10 subsets and tested with the remaining subset such that each of the 10 subsets was used once as a validation set. All 10 sets of validation results were then averaged to produce a single estimation of model performance, measured by the coefficient of determination (R^2, Eq. (2)) and Root Mean Square Error (RMSE, Eq. (3)),

$$R^2 = 1 - \frac{\sum_{i=1}^{n}(y_i - \hat{y}_i)^2}{\sum_{i=1}^{n}(y_i - \bar{y})^2} \quad (2)$$

$$RMSE = \sqrt{\sum_{i=1}^{n}\frac{(y_i - \hat{y}_i)^2}{n}} \quad (3)$$

where n is number of samples, y_i is the PBAR of the ith reference plot, $\hat{y}_i$ is the predicted PBAR of the ith plot, and $\bar{y}$ is the mean PBAR for all the n sample plots.

7 southeastern states, 4 FIA regions and 1 CONUS models were evaluated using this approach. Individual state-level models were not built or assessed for the remaining 41 states, most of which have less than 100 usable reference plots (Table 1). Because the FIA plots used in this study were selected to address the issues described in section 2.2.3, the resultant validation results likely will be different from those derived using a design-based approach (Olofsson et al., 2014; Stehman and Czaplewski, 1998), especially in regions where the number of reference plots is less than optimal. However, because the validation plots were not used in training and had little or no spatial autocorrelation with the training plots (FIA plots are located at least 5 km apart from each other), those validation results should provide a reasonably realistic assessment of the models and derived data products. After the model accuracy assessment (see discussion in 4.1), the national model was used to produce wall-to-wall annual disturbance intensity maps for CONUS from 1986 to 2015, where each annual map shows the PBAR values for disturbances from a specific year. In addition to the cross validation described in section 2.2.4, the derived national maps were also evaluated by examining these annual maps over many locations across CONUS where pre- and post-disturbance Google Earth images are available. The high spatial resolution of Google Earth imagery made it possible to determine disturbance intensity qualitatively by examining the pre- and post-disturbance images visually (see Fig. 5). In total 320 random locations were examined, with 80 in each of the four FIA regions. In each region, points were drawn from two categories, 40 from pixels mapped as low-medium intensity class (0– 80%), and 40 from pixels mapped as high intensity class (>80%). The mapped class at each location was compared to the GE imagery pre- and post-disturbance conditions to identify obvious errors (actual low-medium estimated as high, actual high estimated as low-medium).

2.2.5. *Spatial/temporal analysis of the disturbance intensity products*

The annual disturbance intensity maps derived above provided an opportunity to examine the spatial-temporal patterns of disturbance intensity across CONUS over multiple decades. To evaluate the spatial patterns, we aggregated the 30 annual maps into a time-integrated map that records the PBAR of the largest disturbance. This time-integrated map provides a picture of the spatial variability of PBAR at the 30 m spatial resolution. From the annual maps, we also calculated the mean PBAR values at both the state scale and the Environmental Protection Agency (EPA) level 3 ecoregion scale. EPA ecoregions are defined as areas that share regional similarities in the mosaic of biotic, abiotic, terrestrial, and aquatic ecosystem components (Omernik, 1987, 2004), and therefore natural forests within an ecoregion are expected to develop and grow in similar environments. The level 3 ecoregions (EPA, 2006) were used in this study because they appeared to be more appropriate than those at other levels for illustrating the spatial-temporal patterns of forest disturbance intensity mapped in this study. Since the proportion of clear-cut areas to all harvested areas is often used as an indicator of harvest intensity at the regional scale (Mikoláš et al., 2015; Schleeweis et al., 2020; Soutiere, 1979), we also examined the spatial variability of stand-clearing disturbances across states and ecoregions. Stand clearing is defined as no less than 80% basal area removal (Birdsey and Lewis, 2002).

To examine the temporal variability of disturbance intensity, we used the annual disturbance intensity maps to calculate the mean PBAR as well as the proportion of stand clearing area (PSCA) per each of the 30 years for each state, each ecoregion, and CONUS. PSCA is calculated as proportion of stand-clearing area to total disturbance area. The produced time series allow for investigations into the temporal trend of disturbance intensity. Preliminary analysis indicated there could be three types of temporal changes: trends with a turning point in the middle and similar levels of PBAR at the two ends of the study period (i.e., increase followed by decrease or decrease followed by increase), near monotonic increasing or decreasing trends, and no obvious trend.

A two-step process was used to determine the change type of a time series. First a second-order polynomial regression model ($ax^2 + bx + c$) was used to test if there were trends with a turning point. If the p-value of t-test indicates the polynomial regression was statistically significant (p

< 0.01), a positive quadratic term (coefficient a) would indicate initial decrease followed by increase in PBAR and/or PSCA, while the opposite (initial increase followed by decrease) would have a negative coefficient. Given the relatively short record (30 years) of the disturbance intensity time series, higher order polynomial models were not considered in this study. Therefore, a time series would have no obvious trend if it failed the *t*-tests of both the linear and 2nd order polynomial fitting. Then the turning point of the polynomial regression model was calculated to determine if the trend had a turning point in the middle and similar levels of PBAR at the two ends of the study period, or if the trend had near monotonic increasing or decreasing with a turning point outside the study period.

3. Results

3.1. Model performance at different scales

The disturbance intensity mapping algorithm appeared to be robust for most of the seven southeastern states. The cross-validation results (comparison of predicted values against reference data for samples not used in model calibration) resulted in R^2 values ranging from 0.55 to 0.80 and RMSE from 13% to 18% (Fig. 3). Model results derived over the four US regions and CONUS were not as good as those derived over AL and other 4 southeastern states, but they were comparable to those derived over MS and TN (Fig. 4). These regional and national models made it possible to map PBAR across CONUS despite the difficulty in developing separate mapping models for individual states due to the lack of adequate sample plots for model development in many states. In particular, the accuracy of the national model appeared to be similar to those derived over the Southern Region (SR) and Pacific Northwest (PNW) regions and better than those over the Interior West (IW) and Northern Region (NR), suggesting that the national model could be robust enough for mapping PBAR across CONUS. Therefore, the national model was used to produce the final wall-to-wall PBAR maps annually across the country.

Since the accuracy values of the national model shown in Fig. 4 were derived using set-aside plots that had essentially no spatial autocorrelation with those used in model calibration (FIA plots are located at least 5 km apart from each other), they should provide a reasonably realistic representation of the accuracies of the derived annual PBAR maps at the national scale. While the accuracy of the national model might be driven by plots in the SR region, which contributed 44% of the plots used in this study, no obvious regional biases were found during our comprehensive visual assessments of the resultant maps against available high resolution Google Earth images. The mapped PBAR values appeared reasonable in most of the areas we checked. Fig. 5 provides a few visual assessment examples for different disturbance types in different regions.

In the examination against GE Imagery, of the total 160 locations with estimated low-medium intensity over the four FIA regions, 90% in PNW, 85% in IW, 82.5% in NR and 97.5% in SR appeared to have experienced low-medium intensity disturbances; for the 160 locations with estimated high intensity, 92.5% in PNW, 87.5% in IW, 95% in NR and 95% in SR appeared to have experienced high intensity disturbances (Table 2).

3.2. Spatial patterns of disturbance intensity in CONUS

The derived disturbance intensity maps revealed that 513,177 km^2 (19.8%) of the forested lands in CONUS were disturbed at least once. About 284,265 km^2 (55%) of the mapped disturbance areas had stand-clearing disturbance events (defined as $\geq$ 80% PBAR). The time-integrated map created from the annual maps, which represents the PBAR value of largest disturbance, shows how well the spatial patterns of PBAR match the boundaries of many ecoregions (Fig. 6). As expected, the highest disturbance intensities were found in several ecoregions in the Southeast, Lower South, and Pacific Northwest, where industrial forests with heavy timber harvests are located. Fire disturbance intensity in the West was highly variable, where moderately high disturbance intensities were found in many ecoregions along the coast and near the Rockies, while most other areas had moderate to low disturbance

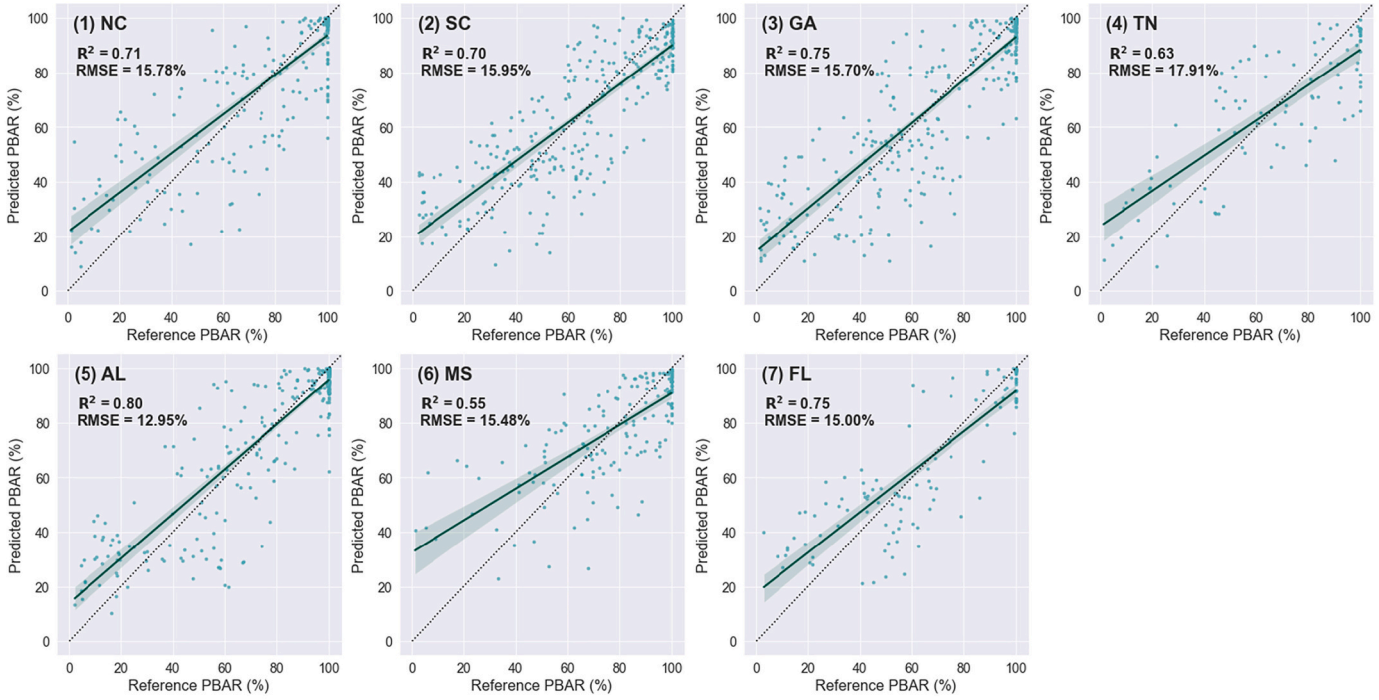

Fig. 3. Validation of disturbance intensity mapping models developed for seven southern states using set aside reference plots not used in model calibration (notes: unit of histograms on the side is the count of plots; green solid line is the fitted line; black dashed line is the 1:1 line). (For interpretation of the references to colour in this figure legend, the reader is referred to the web version of this article.)

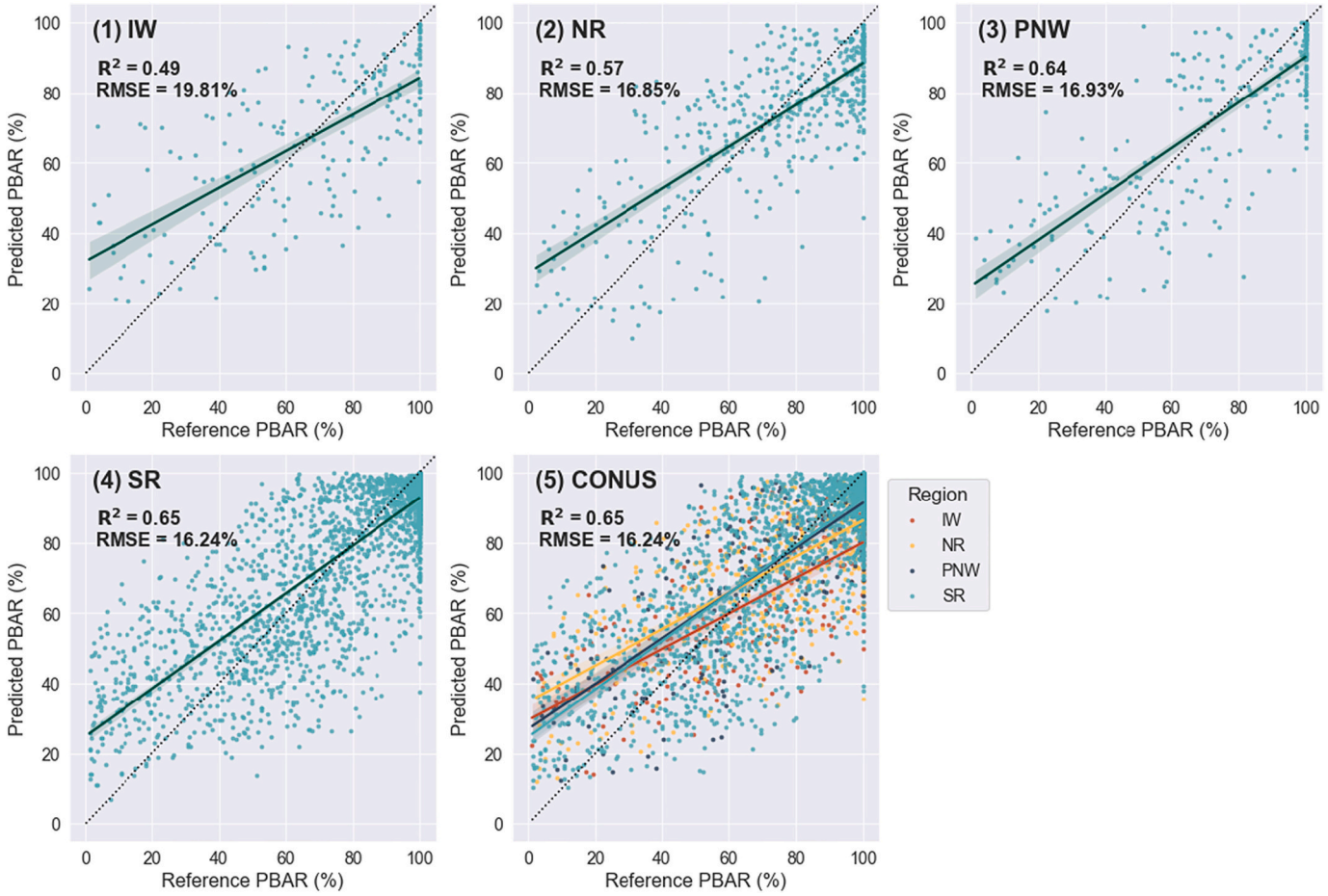

Fig. 4. Validation of disturbance intensity mapping models developed for (1) Interior West (IW) Region; (2) Northern Region (NR); (3) Pacific Northwest (PNW) Region; (4) Southern Region (SR); and (5) CONUS using set aside reference plots not used in model calibration (notes: unit of histograms on the side is the count of plots; green solid line is the fitted line; black dashed line is the 1:1 line). (For interpretation of the references to colour in this figure legend, the reader is referred to the web version of this article.)

intensities.

At the state level, 30-year mean PBAR ranged from 52% to 81% (Fig. 7-A). The southeastern states, two states on the pacific northwestern coast (WA and OR), as well as VA and DE have the highest mean PBAR. Several states in the West, including CA, ID, MT, and NV, and two in the east (ME and MD) had moderate disturbance intensities, while values in the remaining states were relatively low.

The ecoregion-based mean PBAR map shows that the disturbance intensity had large within-state variations (Fig. 7-B). In both WA and OR, for example, high PBAR is seen in the western ecoregions including Coast Range, Willamette Valley, and Cascades, while forestlands to the east of Cascade Range experience low- to medium-intensity disturbances. In California, the Coast Range and Central California Valley ecoregions have much higher mean PBAR (i.e., 82% and 76%) than other regions within the state. Such spatial variability also exists in Texas, where high values only exist in the two ecoregions in the east and west of the state, South-Central Plains and High Plains. For the southeastern US, where the state-level mean PBAR was high, exceptions can be seen in ecoregions such as the Mississippi Alluvial Plain, Southern Florida Coastal Plain, and Western Gulf Coastal Plain. These ecoregions are primarily dominated by land cover types other than forest land, such as crops and pastureland, grassland, and wetland (Homer et al., 2020). Mid- to low- intensity disturbances are also seen in the Blue Ridge region, where national forests and national parks occupy about 50% of the total land area. As expected, the mean PSCA had roughly the same spatial patterns as the mean PBAR but varied in wider value ranges (Fig. 7-C, 7-D). PSCA was lowest in NY (16%) but was over 60% in several southeastern states (e.g., AL, GA, LA) (Fig. 7-C). The value range was slightly larger at the ecoregion level, ranging from 13% to 70% (Fig. 7-D). Ecoregions with high PSCA values include Coast Range and Central California Valley along the Pacific coast and Southeastern Plaines, Piedmont, Middle Atlantic Coastal Plain, and Southern Coastal Plain in the southeast (Fig. 7-D), where clearcutting has been a common practice (Siry, 2002; Smith and Darr, 2004).

3.3. Temporal trends of disturbance intensity

The mapped disturbance intensities had considerable temporal variations. During the 30-year study period, the annual mean PBAR values over CONUS varied between 66% and 77% while the annual mean PSCA ranged from ~40% to 58%. The result reveals that of all disturbed forest area, only around half are stand-cleared, indicating the importance of considering disturbance intensity when calculating disturbance area or disturbance rate. Both the mean PBAR and PSCA had increasing trends during the first half of the study period followed by decreasing trends in the 2nd half after they peaked at around 2003 (Fig. 8). Overall, there is a net increase of 2% in PBAR and 3% in PSCA from 1986 to 2015. It's worth noting that the annual total disturbance area over CONUS did not seem to have any obvious trend and varied over a much wider relative range, from below 20,000 km^2 to above 30,000 km^2 (a range of about 50% of the mean). The temporal range of state level mean annual PBAR, calculated as the difference between the annual mean PBAR values at

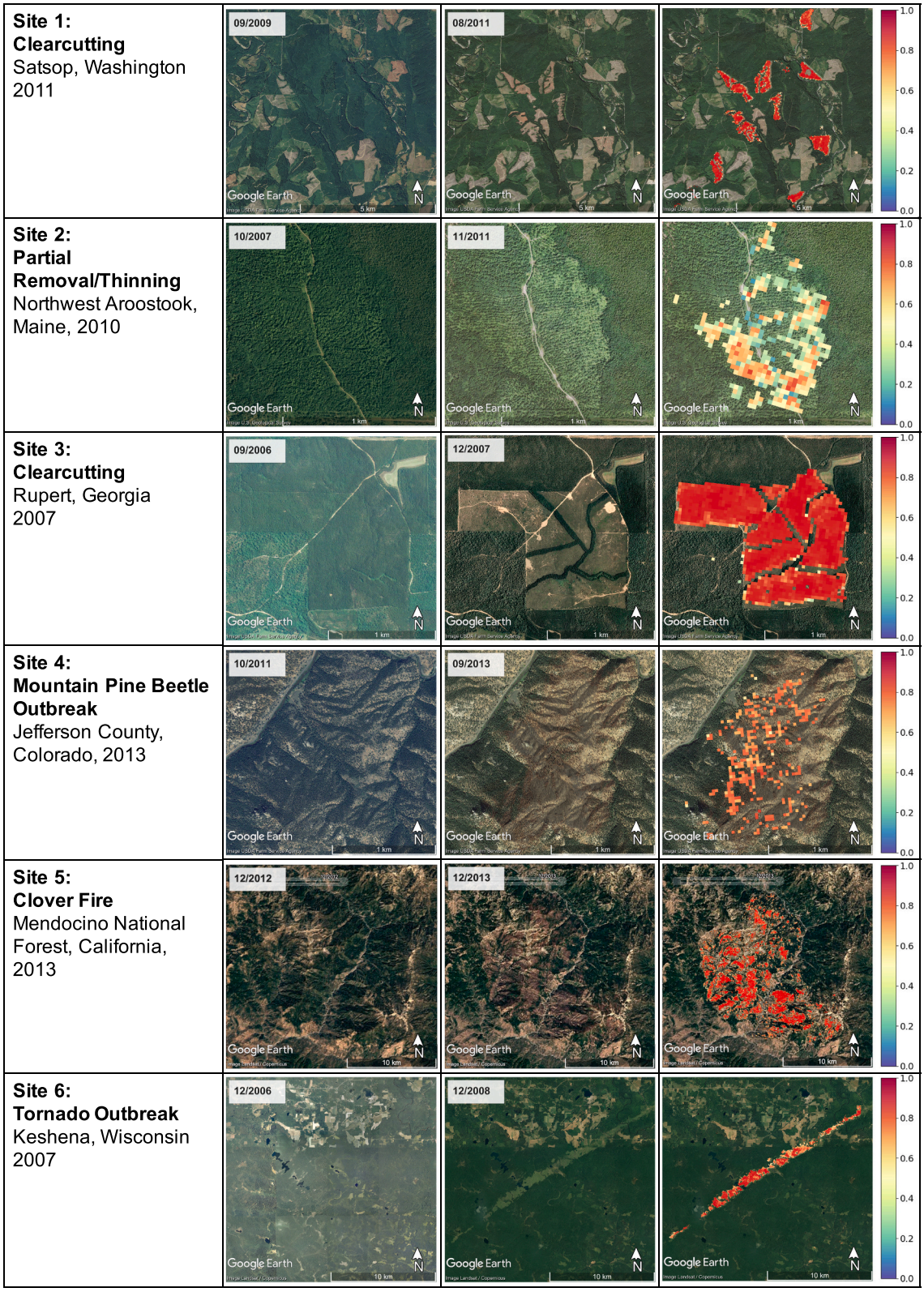

Fig. 5. Qualitative assessment of the derived disturbance intensity maps overlaid on Google Earth images (4th column) by visually examining high resolution Google Earth images acquired before (2nd column) and after (3rd column) the mapped disturbances for different disturbance types selected from across the country. See Fig. 6 for the locations of the selected examples.

Table 2
Visual examination results of mapped intensity over 320 random locations across CONUS with 80 locations in each of 4 FIA regions (Low-medium: PBAR <80%; high: PBAR≥ 80%).

FIA Region		Low-medium (n = 40 for each region)	High (n = 40 for each region)
PNW	Low-medium	36 *(90%)*	3
	High	4	37 *(92.5%)*
IW	Low-medium	34 *(85%)*	5
	High	6	35 *(87.5%)*
NR	Low-medium	33 *(82.5%)*	2
	High	7	38 *(95%)*
SR	Low-medium	39 *(97.5%)*	2
	High	1	38 *(95%)*

the 90th and 10th percentiles of each state, varied from 5% to 21% among the 48 states and from 5% to 23% among the 85 ecoregions. Additionally, the range of mean PSCA varied from 10% to 37% among states and 6% to 50% among ecoregions (Fig. 9). Likely due to large interannual variability in disturbances driven by fire and insect outbreaks (Meigs et al., 2015; Singleton et al., 2019), states and forested ecoregions located in the semiarid west had some of the highest temporal ranges. Most of the remaining states and ecoregions in the country, including those located in the eastern U.S. and along the Pacific coast, had lower temporal variations with their mean PBAR and mean PSCA values.

At the state level (Fig. 10-A), about two thirds (33 out of 48) of the states had annual mean PBAR values that seemed to follow 2nd order polynomial trajectories with negative 2nd coefficients (initial decreasing trends followed by increasing trends towards the end). The remaining 15 states either did not have statistically significant trends or had extremely low forest cover (< 5%) and hence these trends would not be that meaningful. 11 of 33 states that had statistically significant 2nd order trends (AZ, CO, CT, FL, IL, IN, KY, MD, NJ, NM, TN, TX, UT) had a relatively balanced inverse "U" shape with similar levels of PBAR at the two ends of the study period and a turning point around the middle (2000 ± 3 years). The majority (20 out of 33) had increasing trends throughout much of the study period that resulted in substantially higher disturbance intensities during the later years than the earlier years of the study period (Fig. A1). Large increase (>10%) in PBAR was seen in several states (e.g., VA, AR, and MN). Two states (VA, VT) had turning points beyond 2015, meaning they had near monotonic increasing trends over the 30-year study period. With a turning point in 1996, only MT had lower mean PBAR values in the 2010s than in the

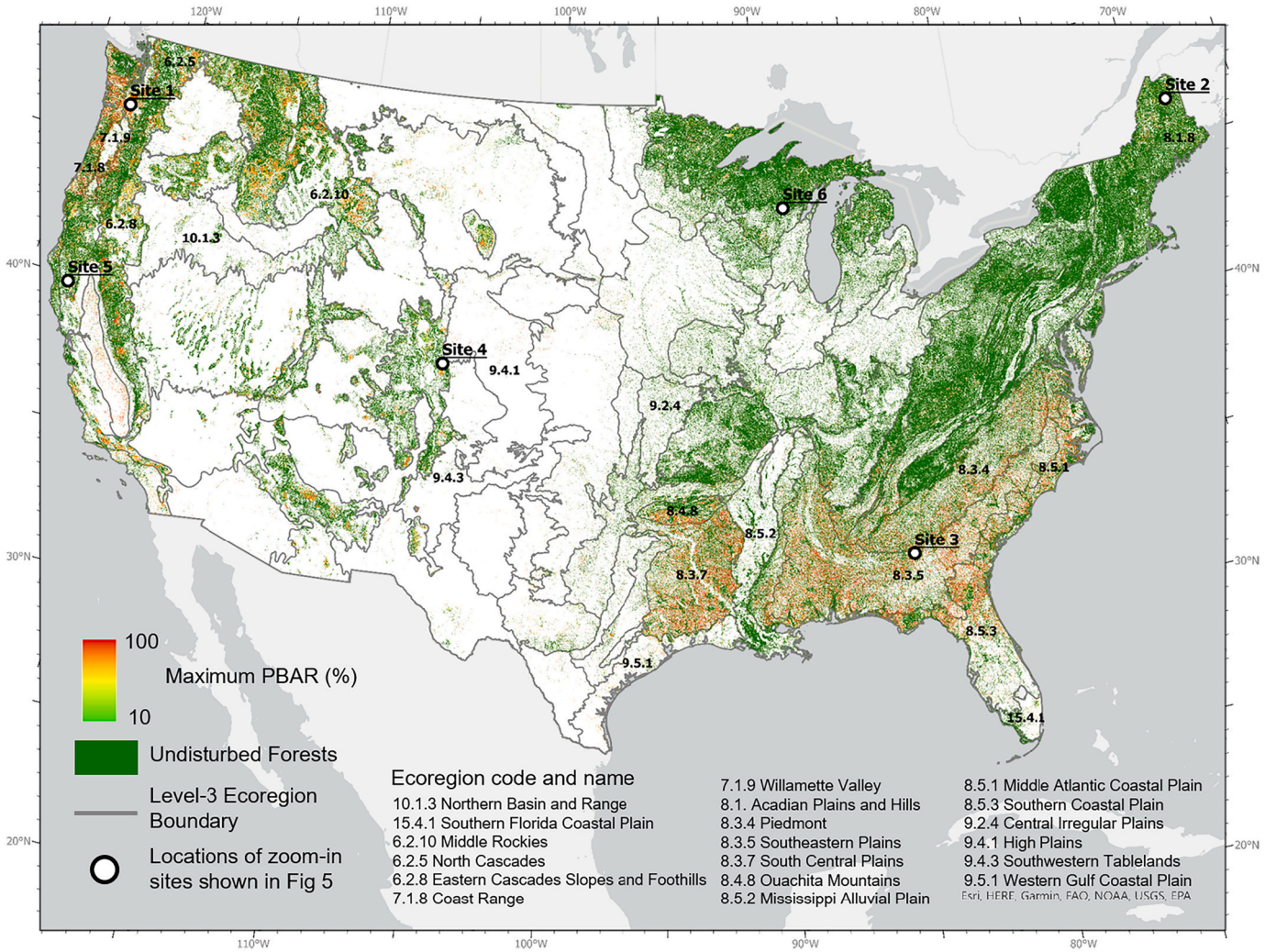

Fig. 6. A time-integrated map representing the percentage of basal area removal (PBAR) value regardless of the disturbance year for pixel locations where only one disturbance event was detected and the maximum PBAR for locations that were disturbed multiple times overlaid with EPA Level 3 ecoregions shows that the spatial patterns of mapped disturbance intensities match the boundaries of many ecoregions.

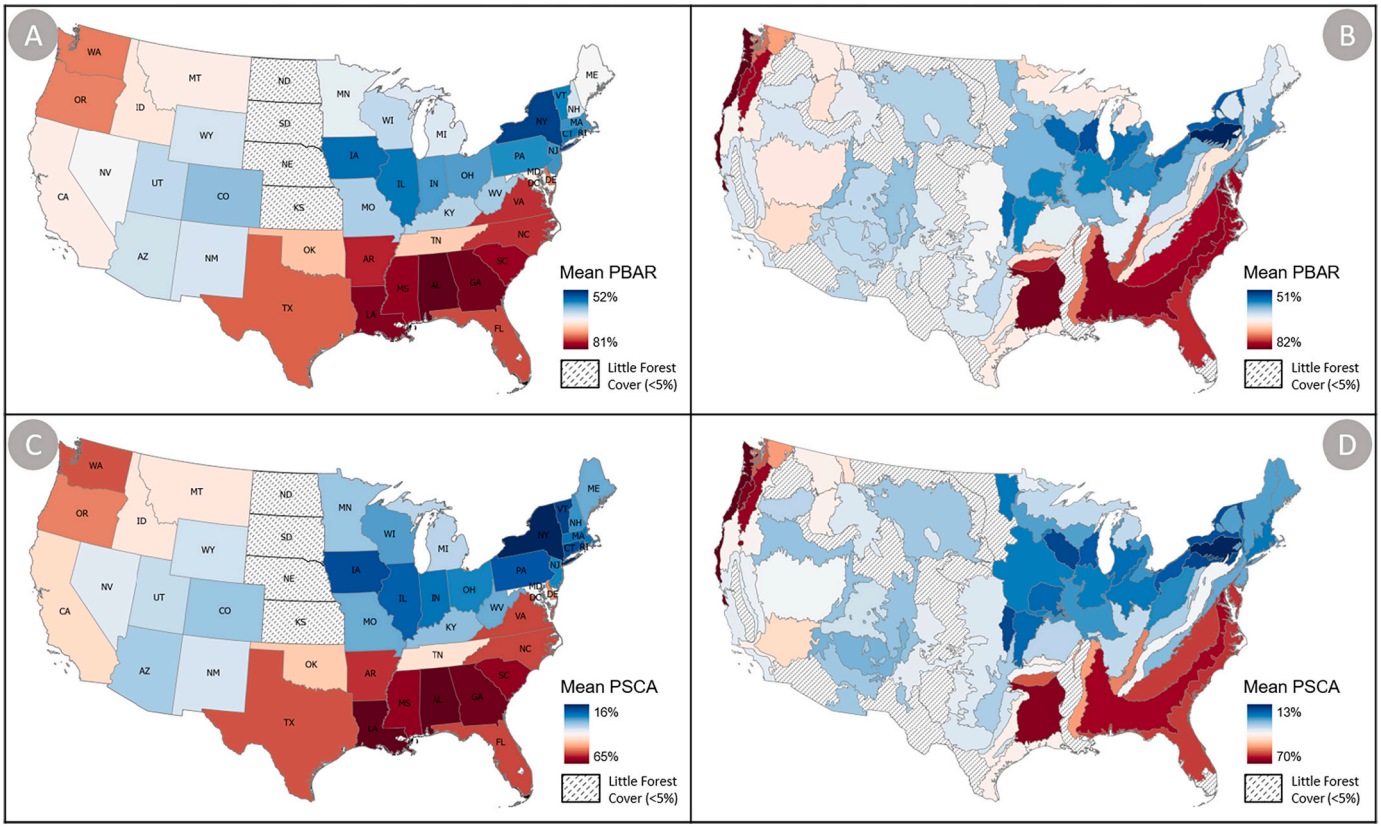

Fig. 7. Spatial pattern of 30-year average percentage of basal area removal (PBAR) (A: by state, B: by EPA level 3 ecoregion) and average proportion of stand-clearing area (PSCA) (C: by state, D: by EPA level 3 ecoregion).

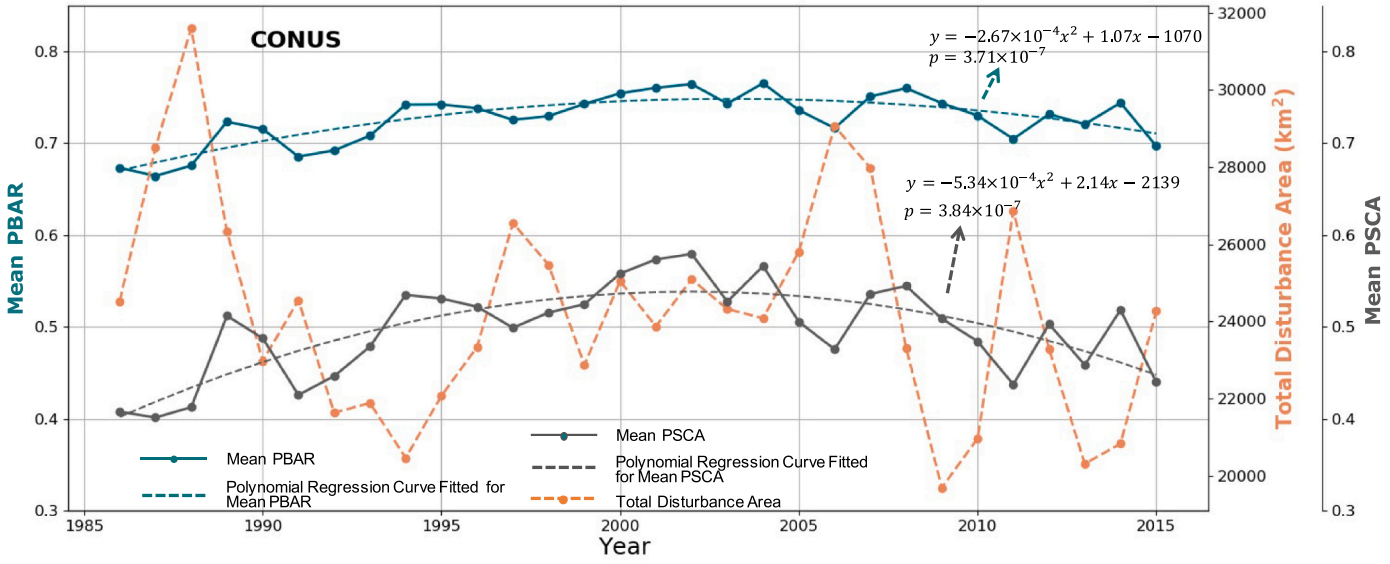

Fig. 8. Temporal profile of annual mean PBAR (green solid line), annual mean PSCA (grey solid line), and total disturbance area (orange dashed line); along with second order polynomial trends fitted for annual mean PBAR (green dashed line) and annual mean PSCA (grey dashed line). (For interpretation of the references to colour in this figure legend, the reader is referred to the web version of this article.)

1980s.

While the PBAR temporal trends of many ecoregions were similar to those of the states that intersect or overlap with them, there were a few anomalies (Fig. 10-B). For example, although the state level mean PBAR over WA, OR, CA, and ME did not have any obvious trends, some ecoregions that were completely located within these states, including Coast Range and Acadian Plains and Hills, had near monotonic increasing trends. While none of the states had a trend with a positive 2nd coefficient, three ecoregions, including Eastern Cascades Slopes and Foothills, Ouachita Mountains, and Southwestern Tablelands had positive 2nd coefficients. Large increase (>10%) in PBAR was seen in Northern Minnesota Wetlands, and large decrease (>10%) was observed

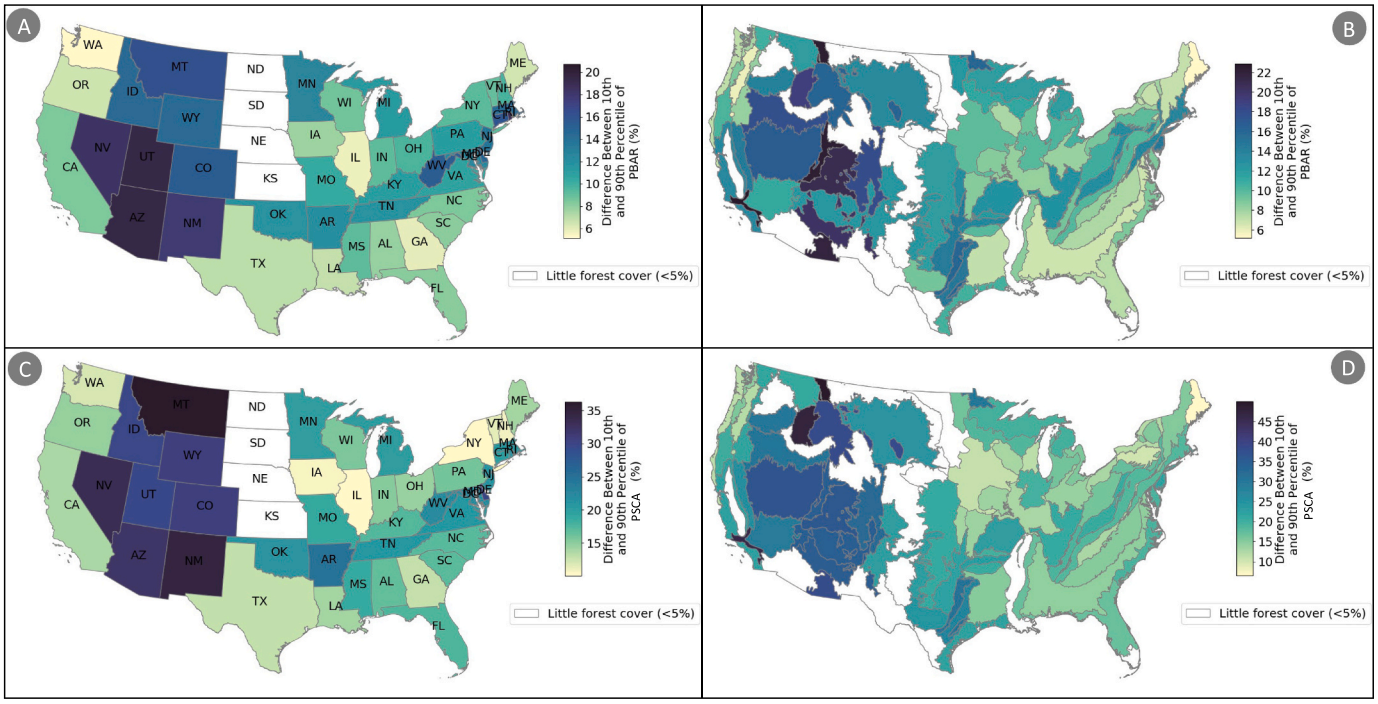

Fig. 9. Temporal range of state level mean annual PBAR calculated as the difference between the annual mean PBAR values (A: of each state; B: of each ecoregion) and PSCA values (C: of each state; D: of each ecoregion) at the 90th and 10th percentiles.

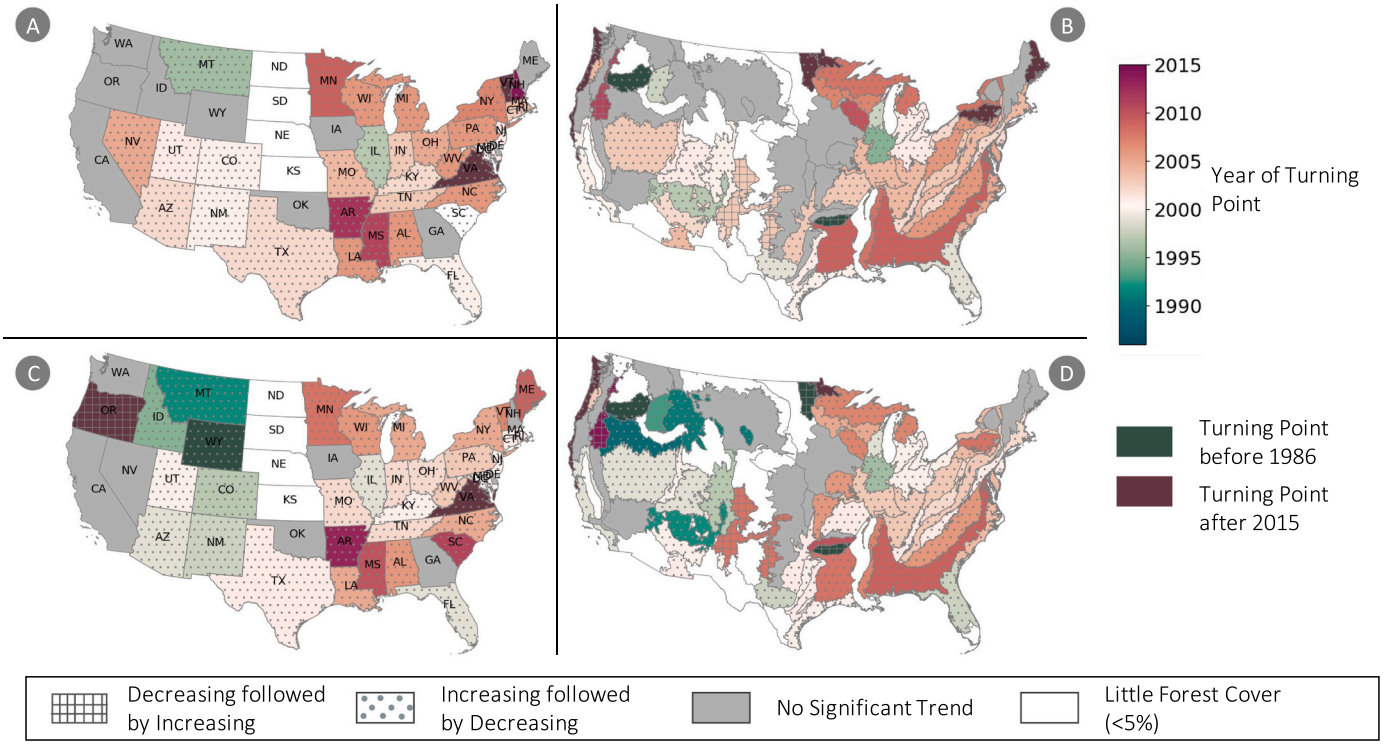

Fig. 10. Temporal trends fitted for PBAR (A: by state, B: by ecoregion) and PSCA (C: by state, D: by ecoregion). Year of turning point is mapped for states/ecoregions with significant polynomial fitting. Point-hatched polygons are states/ecoregions with decreasing followed by increasing trends ("U" shape), while grid-hatched polygons are states/ecoregions with increasing followed by increasing trends (inverse "U" shape). Grey-colored states/ecoregions are where no significant trend is fitted, and white indicates where forest cover is low (less than 5%).

in Blue Mountains (Fig. A2). Locations of ecoregions mentioned are marked in Fig. 6.

Overall, the temporal trends of mean PSCA followed those of mean PBAR at both state and ecoregion levels. However, there were a few states that did not have statistically significant trends with their mean PBAR values, but their mean PSCA values showed 2nd order trends, including ID and WY having negative 2nd coefficients and OR and ME having positive coefficients (Fig. 10-C). On the other hand, NV and NH

had significant trends with their mean BPAR, but not with the mean PSCA. Similarly, several ecoregions, including Northern Basin and Range, Middle Rockies, North Cascades, and Central Irregular Plains did not have obvious trends with their mean PBAR values, but their mean PSCA showed statistically significant trends (Fig. 10-D). The ecoregion that had significant trends with their mean PBAR but not with their mean PSCA values was Acadian Plains and Hills.

4. Discussion

Forest disturbances can have broad impact on the climate, local environment, and the regeneration of the forest ecosystem. The nature and magnitude of such impact, however, is largely driven by disturbance intensity. Previously, we developed an approach for mapping forest disturbance intensity by integrating time series Landsat observations and FIA field inventory measurements in a Random-Forest-based machine learning framework and demonstrated its effectiveness in North and South Carolina (Tao et al., 2019). In this study, we evaluated this approach in seven individual states located in the Southeast, over the four FIA regions that constitute the CONUS, and for the entire CONUS. The feasibility of using a single national model to produce CONUS-wide products was evidenced by the fact that the RF model developed over CONUS was comparable to or even better than the individual models developed for four US regions when evaluated over set-aside samples. With this national model we produced the first set of disturbance intensity maps with a 30-m spatial resolution over the entire CONUS that characterize forest disturbance intensity on an annual basis for a 30-year period.

By quantifying the percentage of basal area removed by disturbance events, these products can provide a much more precise characterization of the full continuum of severity in basal area loss events. This represents an improvement over categorical maps only flagging whether or not a loss has occurred, and allows for a better understanding of the impact not only on the forests being disturbed, but also on local hydrology, energy balance, habitat, and a suite of other related environmental issues (Banks et al., 2013; Hanson and Lorimer, 2007; Reid et al., 2010; Senf and Seidl, 2021). The annual time step over three decades and the CONUS 30-m spatial resolution coverage, also represent improvements that can provide finer details for up to 30 years over any area within CONUS. The spatial-temporal PBAR patterns in the derived products were in general agreement with Forest Service reports on areas and trends of stand clearing harvest (Siry, 2002; Smith and Darr, 2004). Compared to areas affected by logging events, PBAR mapped over areas affected by natural disturbances, such as fire and insect outbreaks, were more likely to be driven by both the severity of those events and post-disturbance management practices, such as salvage logging (Leverkus et al., 2018; Lindenmayer et al., 2008), A CONUS-wide disturbance attribution map has been developed (Schleeweis et al., 2020). It is possible to combine the PBAR and attribution maps to calculate the loss of basal area from different disturbance types. Further analyses of the temporal trends of the PBAR of different disturbance types may reveal how the drivers of different disturbance types have changed over time. For example, trends in harvesting intensity may reflect changes in forest management practices (Legaard et al., 2015), while trends in natural disturbance events are more likely due to climate change or interdecadal climate variability (Abatzoglou and Williams, 2016; Harris et al., 2018).

Our modeling approach requires both remote sensing time series observations and repeat field measurements provided by the FIA data. Optical systems such as the Landsat satellite series can provide near contiguous observations at national to global scales on near annual or even sub-annual bases (Wulder et al., 2019; Zhu et al., 2019a). While in the past data gaps could arise from constant cloudy conditions in certain regions and/or acquisition limitations due to many practical reasons (Asner, 2001; Ju and Roy, 2008), such gaps should be greatly reduced when global observations acquired by the Sentinel-2 satellites launched in 2015 and 2017 become available. Such observations make it possible to time and map locations of disturbance events as well as spectral changes caused by those events over large areas. Further, the successful launch of the Sentinel-1 satellites in 2014 and 2016 ushered a new era where global systematic acquisitions of Synthetic Aperture Radar (SAR) data have become publicly available (Torres et al., 2012). With a planned launch date in 2023, the NASA-ISRO SAR (NISAR) mission is expected to provide L-band SAR data across the globe (Rosen et al., 2015). In general, SAR data are more sensitive to vegetation structure than optical data (Lu et al., 2016; Treuhaft et al., 2004). Methods for mapping forest disturbances using time series SAR observations have been developed and will continue to evolve (Bouvet et al., 2018; Hirschmugl et al., 2020; Rüetschi et al., 2019).

While optical and SAR data could be used to detect forest disturbances and calculate the change signals caused by those disturbances in satellite observations, field measurements are needed to convert the satellite observations to changes in physical quantities like basal area or biomass. The FIA field inventory database is an invaluable dataset for quantifying forest disturbance intensity across CONUS. The database provides field-based measurements for many basic biophysical quantities such as height, diameter, and age at tree and plot levels (Bechtold and Patterson, 2005; McRoberts et al., 2005). From these measurements other derived quantities such as basal area, volume, and biomass were also calculated (Bechtold and Patterson, 2005; McRoberts et al., 2005). Net changes in these biophysical quantities can be derived by comparing these data through time. However, because FIA plots are revisited at 5- to 10-year intervals, these net changes in general are not the sole results of changes caused by disturbance events that occurred between two field measurements. Fortunately, the FIA database provides adequate information for tracking the same trees measured in different inventory cycles. This information made it possible to calculate the basal area loss caused by disturbances that had occurred between two consecutive field visits (Tao et al., 2019). As discussed in section 2.1.2 and 2.2.3, however, the FIA data needs to be filtered carefully in order to select the plots that could be used to derive reliable PBAR values and minimize the impact of potential misregistration errors between field measurements and satellite observations. As shown in Table 1, this resulted in an extremely limited quantity of useable plots, with valid reference PBAR information, for a few states in the Northern and Interior West regions, which could be a reason why the models developed for these two regions had lower R^2 values than those developed for the other two regions and across CONUS.

One way to mitigate this problem is to intensify field sampling over areas where certain disturbances (e.g., planned harvest) are known to happen ahead of time and collect field measurements before and after those disturbances. For natural disturbances that are often unpredictable, rapidly remeasuring established field plots in and around disturbance affected areas provides useful information (Sheffield and Thompson, 1992; Woodall and Leutscher, 2005). Ideally, remote sensing mapping algorithms need to be calibrated using reference data with spatial and temporal characteristics matching those of remote sensing data. As discussed in many previous studies (e.g. Hoppus et al., 2000; Nelson et al., 2009; Tao et al., 2019), there are considerable spatial-temporal mismatches between FIA measurements and Landsat observations, which likely contributed to some of the mapping uncertainties reported in this study.

Given the fact that lidar has become a locally viable alternative to field methods for measuring many forest attributes (e.g., canopy, height, etc.) (Lefsky et al., 2002; Matasci et al., 2018; Wulder et al., 2012), it may be possible to use lidar data to derive reference data required for disturbance intensity mapping. Depending on how fast trees can grow or regenerate in a study region, however, multi-temporal lidar data acquired within a short period (e.g., 1–2 years) would be needed to derive reliable reference disturbance intensity data. Such data could be obtained by acquiring new lidar data over areas that were disturbed recently and had old lidar or ground measurements acquired shortly before disturbance. Finding such areas may have been difficult in the

past. Now that the GEDI (Global Ecosystem Dynamics Investigation) (Dubayah et al., 2020) and ICESat2 (Ice, Cloud, and land Elevation Satellite-2) (Neuenschwander and Pitts, 2019) are acquiring lidar samples across the globe, and airborne lidar data are acquired for increasingly more areas (Sugarbaker et al., 2014), there are more opportunities to obtain repeat lidar measurements within a year or two of disturbance events. As discussed in section 2.2.3, due to potential tree growth and/or regeneration between those measurements, the difference between two lidar measurements acquired many years apart cannot be attributed solely to changes caused by disturbances that had occurred between the two measurements. The method we developed for calculating PBAR by tracking individual trees over time with FIA plot data, likely cannot be adapted for use with lidar data, because it is not possible to identify individual trees using large footprint waveform lidar data, and tree delineation using very dense lidar cloud point data remains a challenge (Aubry-Kientz et al., 2019; Zhang et al., 2015).

Despite the simplicity and convenience as well as some of the advantages of using a single national model to map disturbance intensity across CONUS, the fact that mapping models developed for 5 of the 7 southeast states performed better than the national model (Fig. 3) demonstrated that should geographically representative reference data be available for all states or ecoregions, improved disturbance mapping could be achieved by using a collection of state- or ecoregion-based mapping models instead of a single national model. Of course, ample overlap should be provided between adjacent states or ecoregions to reduce potential discontinuities between them. Use of a set of locally calibrated models distributed over a large area has become an increasingly more common practice to improve mapping results at national to global scales (Potapov et al., 2021).

5. Conclusions

By integrating field plot measurements collected by the FIA program and time series Landsat observations, we have produced the first set of annual forest disturbance intensity map products quantifying the percentage of basal area removal (PBAR) at the 30-m resolution for the conterminous United States from 1986 to 2015. These products were generated using a Random Forest model that had an R^2 of 0.65 and RMSE of 16.2% when evaluated using plots not used in model calibration. Comprehensive qualitative visual assessments of annual disturbance intensity maps appeared reasonable when compared to high temporal and spatial resolution Google Earth imagery. The derived map products revealed that during the 30-year study period, the annual average PBAR values of all disturbed pixels across CONUS ranged from 66% to 70%, and the proportion of those pixels having stand-clearing disturbances ranged from 40% to 58%. High disturbance intensity values were concentrated in the Southeastern states from TX to VA and along the Pacific coast and the Cascades in the West. At the national scale, the annual mean disturbance intensity values appeared to follow 2nd order trajectories starting with increasing trends at the beginning and decreasing trends towards the end, along with turning points around 2003. The temporal trends of disturbance intensity differed substantially among many states and ecoregions. While the mean disturbance intensity values for some states and ecoregions did not show obvious trends, most of the states' and ecoregions' disturbance intensity values presented statistically significant 2nd order trends. In particular, several states and ecoregions had near monotonic increasing trends that peaked near the end of the study period or did not reach peak value during the study period. Compared to other published disturbance products, the maps derived through this study can provide unique information on forest disturbance – quantitative estimates of the intensity of mapped disturbance events, which were previously unavailable but are critical for understanding forest dynamics across CONUS over multiple decades. The temporal dynamics of disturbance intensity revealed by these map products may shed light on how forest management practices and other disturbance processes causing basal area loss might have changed across the country. The disturbance intensity data product is available from an ORNL DAAC web portal at https://doi.org/10.3334/ORNLDAAC/2059.

Credit author statement

Jiaming Lu conceptualized the study, developed the methodology, conducted the analysis, and led the writing of the paper. Chengquan Huang formulated the concept, supervised the development of methodology, guided the writing of paper and helped with reviewing and editing. Xin Tao helped with the theoretical development of the work and provide insights on methods relating field data and remote sensing data. Weishu Gong contributed to the reviewing and editing. Karen Schleeweis provided comments and content on the FIA database and associated past studies, and many helpful comments and edits to the paper.

Declaration of Competing Interest

The authors declare that they have no known competing financial interests or personal relationships that could have appeared to influence the work reported in this paper.

Acknowledgement

Building on the NAFD (North American Forest Dynamics) research, a core project of the North American Carbon Program (NACP), this study was made possible by NASA's Carbon Cycle Science and Land Cover and Land Use Change Programs (grants NNX14AM39G, NNX14AD89G, and NNX15AE79G). Additional support was provided by the Department of Geographical Sciences of the University of Maryland and the Laboratory of Environmental Model and Data Optima (EMDO). A large portion of the data processing was performed using the NASA Earth eXchange (NEX) system, which was facilitated by Jennifer Dungan, Andrew Michaelis and their colleagues at NASA Ames Research Center. Use of FIA plot location data was made possible through a Material Transfer Agreement (MTA) established under the leadership of Justin Holgerson and Elizabeth Burrill of the US Forest Service. We thank David Loebman and Moying Li for helping polish the manuscript, and Jack (Jianguo) Ma for his long-term support.

Appendix A. Methods for calculating spectral change indices

For each image in the LTSS, the VCT algorithm determined the forest likelihood of each pixel by thresholding two spectral indices, integrated forest z-score (IFZ) (Eq. (A1)) and normalized difference vegetation index (NDVI) (Eq. (A2)).

$$IFZ = \sqrt{\frac{1}{3}\sum_{band\ red,swir1,swir2}\left(\frac{B_i - \overline{B_i}}{SD_i}\right)^2} \tag{A1}$$

$$NDVI = \frac{B_{nir} - B_{red}}{B_{nir} + B_{red}} \tag{A2}$$

where B_i is the reflectance value of Landsat band i, and $\overline{B_i}$ and SD_i are the mean and standard deviation of band i reflectance for all forest samples identified within an image. Previous study (Tao et al., 2019) indicates that the use of all 10 magnitudes of both types would achieve better model accuracy, and thus all the 10 magnitude variables were calculated in this study.

$$NBR = \frac{B_{nir} - B_{swir2}}{B_{nir} + B_{swir2}} \tag{A3}$$

$$NDMI = \frac{B_{nir} - B_{swir1}}{B_{nir} + B_{swir1}} \tag{A4}$$

$$B4FZ = \frac{B_{nir} - \overline{B_{nir}}}{SD_{nir}} \tag{A5}$$

$$B5FZ = \frac{B_{swir1} - \overline{B_{swir1}}}{SD_{swir1}} \tag{A6}$$

Table A1
Spectral change indices used in disturbance intensity mapping.

Category	Equation	Index
Delta	$magnitude_{\Delta} = Index_{post} - Index_{pre}$	IFZ, NDVI, NBR, B4FZ, B5FZ
Normalized Ratio (NR)	$magnitude_{NR} = 1 - Index_{pre}/Index_{post}$	IFZ, B5FZ
	$magnitude_{NR} = 1 - Index_{post}/Index_{pre}$	NDVI, NBR, NDMI

Appendix B. Temporal Profiles of PBAR in CONUS states and ecoreigons

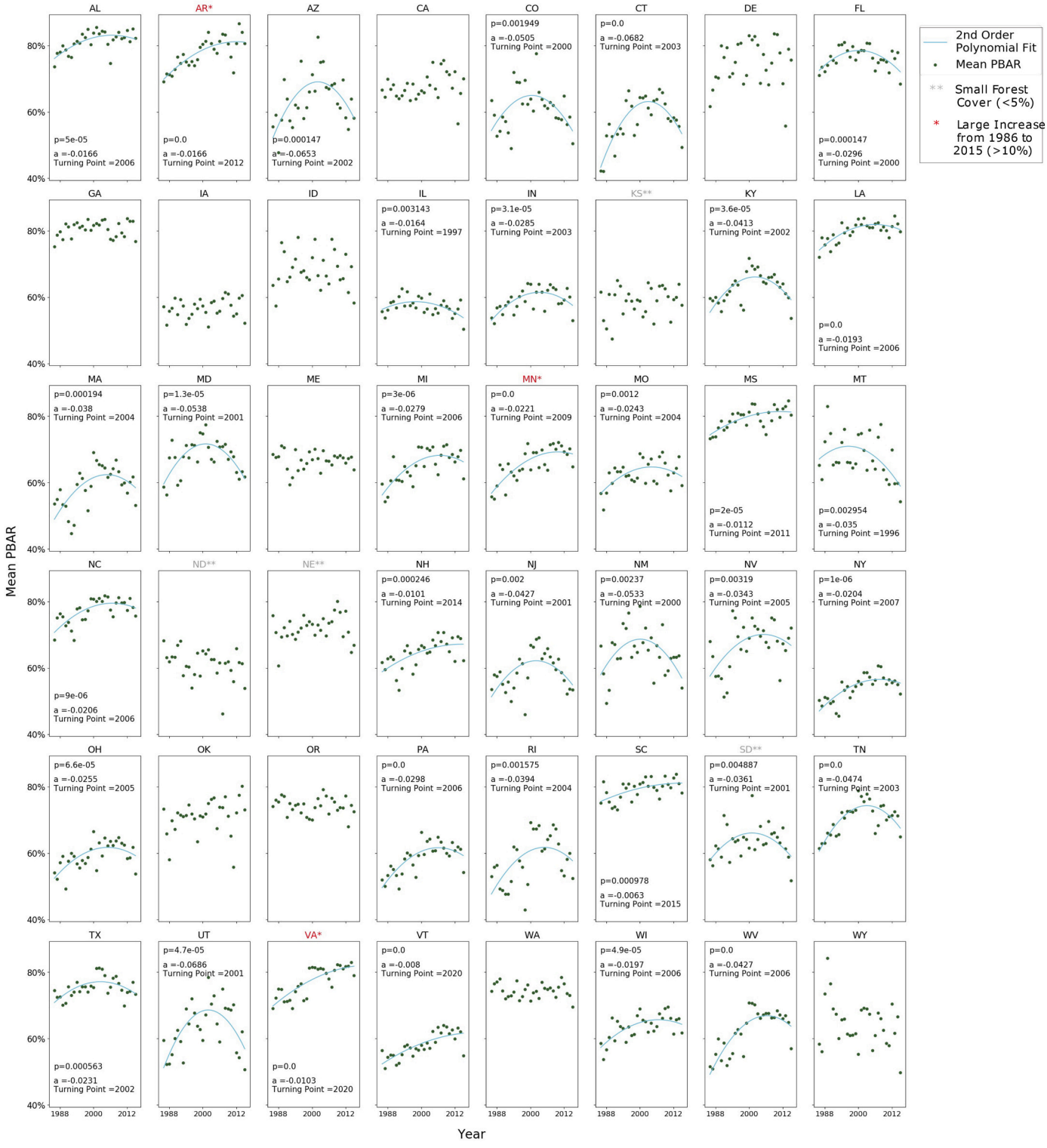

Fig. A1. Temporal profiles of average PBAR in CONUS states. Second order polynomial trend lines (blue curve) are plotted where significant trend is fitted. (For interpretation of the references to colour in this figure legend, the reader is referred to the web version of this article.)

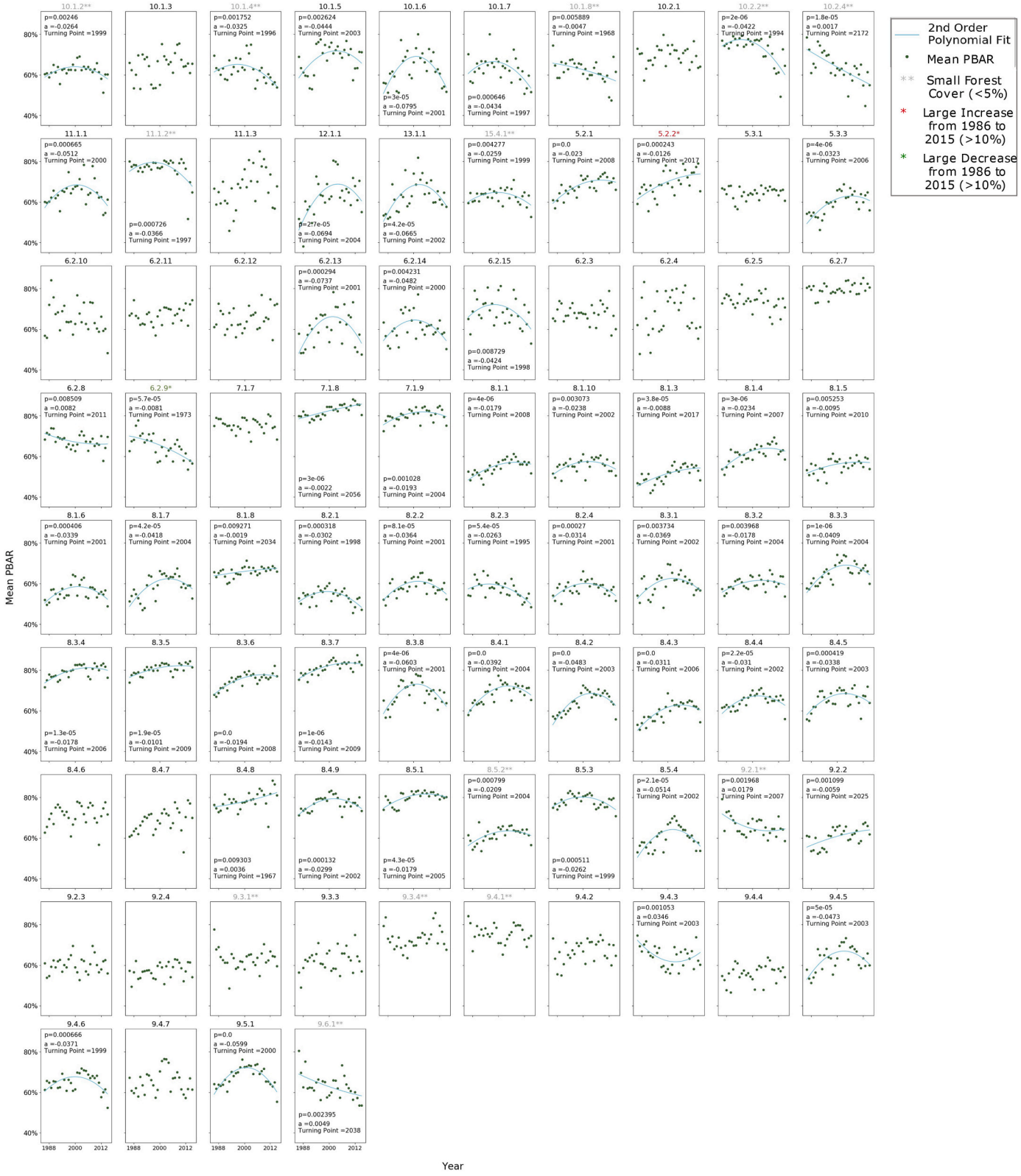

Fig. A2. Temporal profiles of mean PBAR in level-3 ecoregions. Second order polynomial trend lines (blue curve) are plotted where significant trend is fitted. Plots are titled by North America level 3 ecoregion codes (see Table A2 for a list of codes and ecoregion names). (For interpretation of the references to colour in this figure legend, the reader is referred to the web version of this article.)

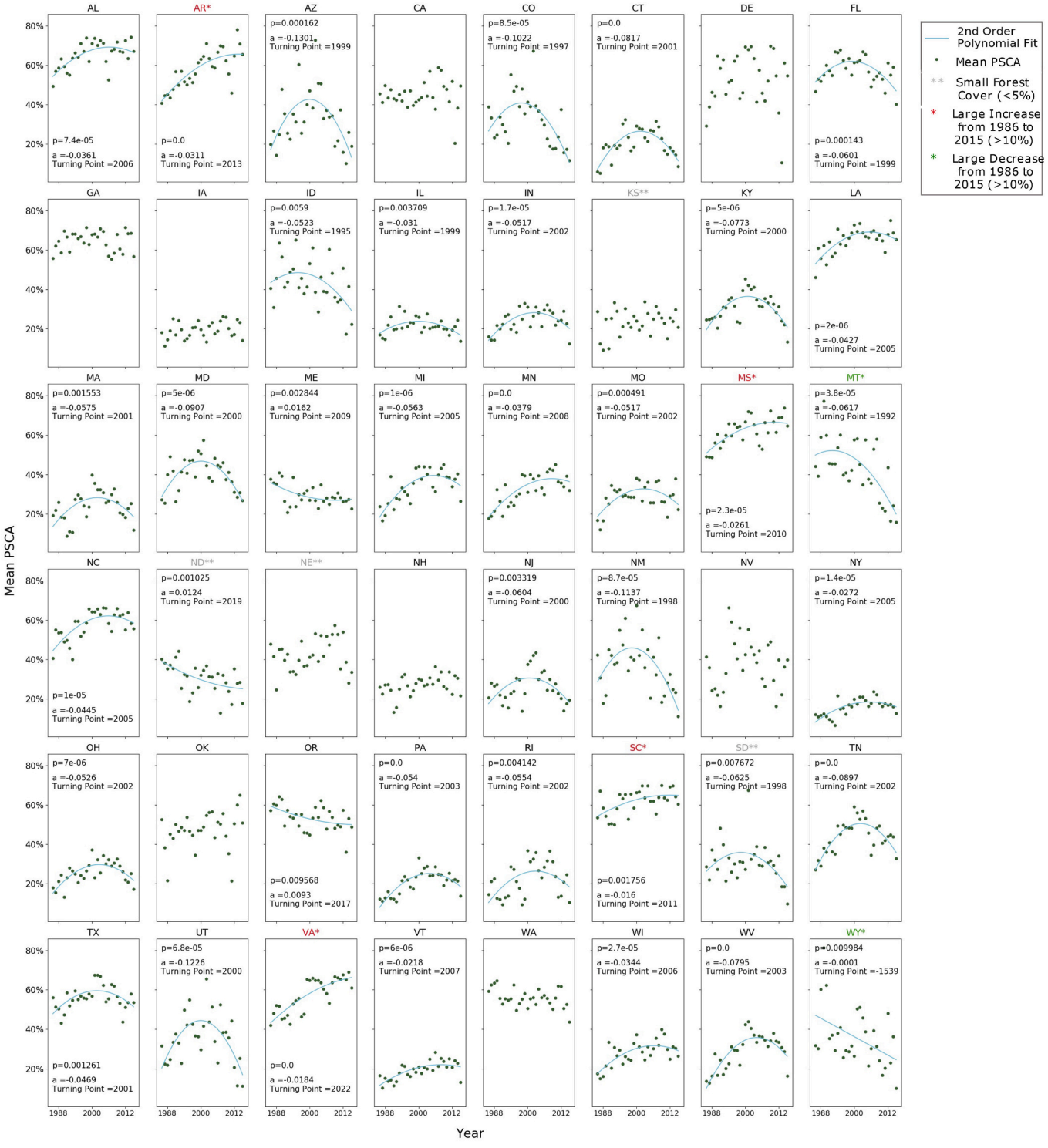

Fig. A3. Temporal profiles of average PSCA in CONUS states. Second order polynomial trend lines (blue curve) are plotted where significant trend is fitted. (For interpretation of the references to colour in this figure legend, the reader is referred to the web version of this article.)

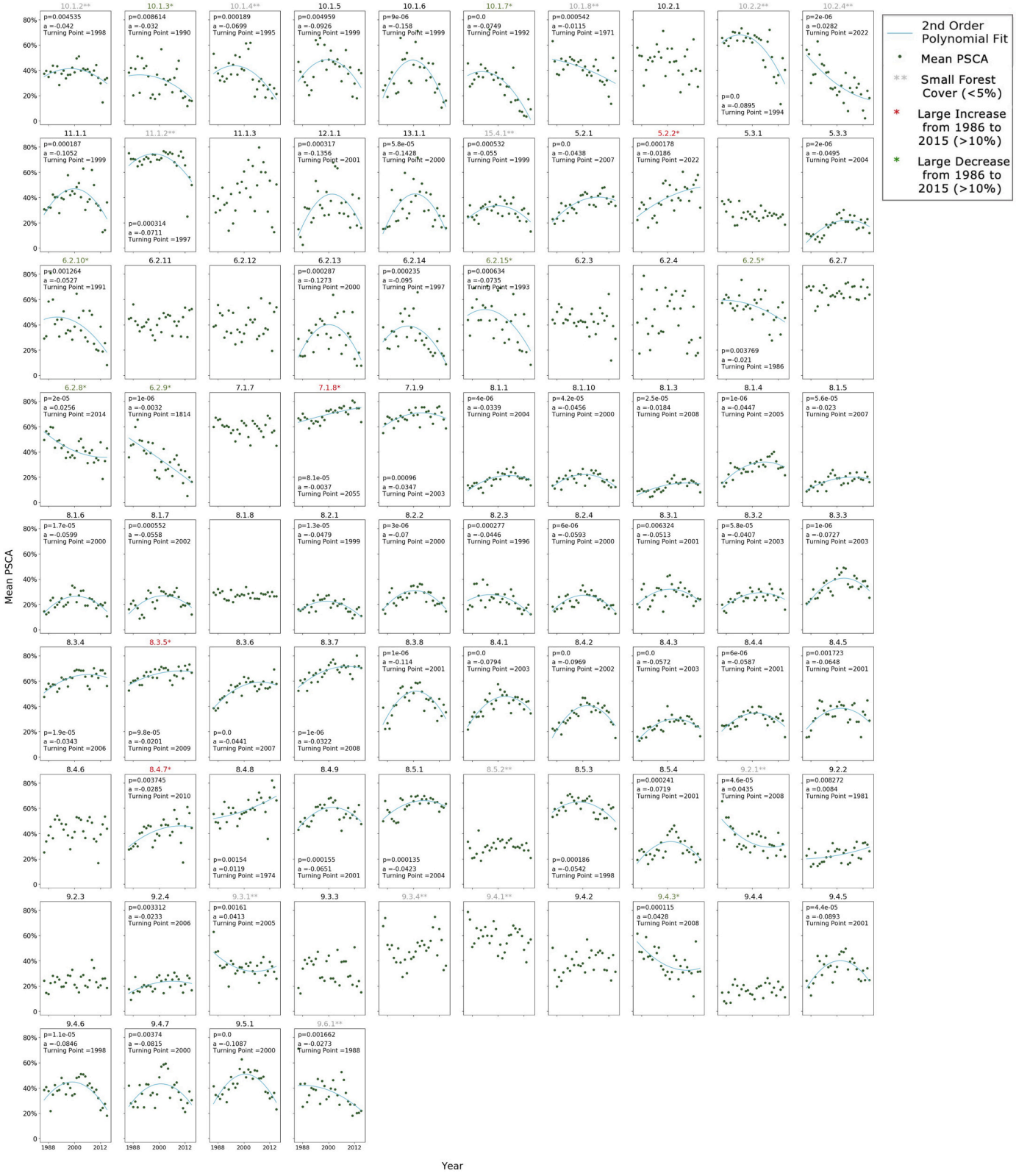

Fig. A4. Temporal profiles of mean PSCA in level-3 ecoregions. Second order polynomial trend lines (blue curve) are plotted where significant trend is fitted. Plots are titled by North America level 3 ecoregion codes (see Table A2 for the list of codes and ecoregion names).
North American Level 3 Ecoregion Codes and Names. (For interpretation of the references to colour in this figure legend, the reader is referred to the web version of this article.)

Table A2
North American Level 3 Ecoregion Codes and Names (see the link for the full ecoregion map: https://gaftp.epa.gov/EPADataCommons/ORD/Ecoregions/cec_na/NA_LEVEL_III.pdf).

CODE	NA_L3NAME	CODE	NA_L3NAME
10.1.2	Columbia Plateau	8.1.8	Acadian Plains and Hills
10.1.3	Northern Basin and Range	8.2.1	Southeastern Wisconsin Till Plains
10.1.4	Wyoming Basin	8.2.2	Huron/Erie Lake Plains
10.1.5	Central Basin and Range	8.2.3	Central Corn Belt Plains
10.1.6	Colorado Plateaus	8.2.4	Eastern Corn Belt Plains
10.1.7	Arizona/New Mexico Plateau	8.3.1	Northern Piedmont
10.1.8	Snake River Plain	8.3.2	Interior River Valleys and Hills
10.2.1	Mojave Basin and Range	8.3.3	Interior Plateau
10.2.2	Sonoran Desert	8.3.4	Piedmont
10.2.4	Chihuahuan Desert	8.3.5	Southeastern Plains
11.1.1	California Coastal Sage, Chaparral, and Oak Woodlands	8.3.6	Mississippi Valley Loess Plain
11.1.2	Central California Valley	8.3.7	South Central Plains
11.1.3	Southern and Baja California Pine-Oak Mountains	8.3.8	East Central Texas Plains
12.1.1	Madrean Archipelago	8.4.1	Ridge and Valley
13.1.1	Arizona/New Mexico Mountains	8.4.2	Central Appalachians
15.4.1	Southern Florida Coastal Plain	8.4.3	Western Allegheny Plateau
5.2.1	Northern Lakes and Forests	8.4.4	Blue Ridge
5.2.2	Northern Minnesota Wetlands	8.4.5	Ozark Highlands
5.3.1	Northern Appalachian and Atlantic Maritime Highlands	8.4.6	Boston Mountains
5.3.3	North Central Appalachians	8.4.7	Arkansas Valley
6.2.10	Middle Rockies	8.4.8	Ouachita Mountains
6.2.11	Klamath Mountains	8.4.9	Southwestern Appalachians
6.2.12	Sierra Nevada	8.5.1	Middle Atlantic Coastal Plain
6.2.13	Wasatch and Uinta Mountains	8.5.2	Mississippi Alluvial Plain
6.2.14	Southern Rockies	8.5.3	Southern Coastal Plain
6.2.15	Idaho Batholith	8.5.4	Atlantic Coastal Pine Barrens
6.2.3	Columbia Mountains/Northern Rockies	9.2.1	Aspen Parkland/Northern Glaciated Plains
6.2.4	Canadian Rockies	9.2.2	Lake Manitoba and Lake Agassiz Plain
6.2.5	North Cascades	9.2.3	Western Corn Belt Plains
6.2.7	Cascades	9.2.4	Central Irregular Plains
6.2.8	Eastern Cascades Slopes and Foothills	9.3.1	Northwestern Glaciated Plains
6.2.9	Blue Mountains	9.3.3	Northwestern Great Plains
7.1.7	Strait of Georgia/Puget Lowland	9.3.4	Nebraska Sand Hills
7.1.8	Coast Range	9.4.1	High Plains
7.1.9	Willamette Valley	9.4.2	Central Great Plains
8.1.1	Eastern Great Lakes Lowlands	9.4.3	Southwestern Tablelands
8.1.10	Erie Drift Plain	9.4.4	Flint Hills
8.1.3	Northern Allegheny Plateau	9.4.5	Cross Timbers
8.1.4	North Central Hardwood Forests	9.4.6	Edwards Plateau
8.1.5	Driftless Area	9.4.7	Texas Blackland Prairies
8.1.6	Southern Michigan/Northern Indiana Drift Plains	9.5.1	Western Gulf Coastal Plain
8.1.7	Northeastern Coastal Zone	9.6.1	Southern Texas Plains/Interior Plains and Hills with Xerophytic Shrub and Oak Forest

References

Abatzoglou, J.T., Williams, A.P., 2016. Impact of anthropogenic climate change on wildfire across western US forests. Proc. Natl. Acad. Sci. 113 (42), 11770–11775.

Akselsson, C., Westling, O., Sverdrup, H., Holmqvist, J., Thelin, G., Uggla, E., Malm, G., 2007. Impact of harvest intensity on long-term base cation budgets in Swedish forest soils. In: Acid Rain-Deposition to Recovery. Springer, pp. 201–210.

Asner, G.P., 2001. Cloud cover in Landsat observations of the Brazilian Amazon. Int. J. Remote Sens. 22 (18), 3855–3862.

Aubry-Kientz, M., Dutrieux, R., Ferraz, A., Saatchi, S., Hamraz, H., Williams, J., Vincent, G., 2019. A comparative assessment of the performance of individual tree crowns delineation algorithms from ALS data in tropical forests. Remote Sens. 11 (9), 1086.

Banks, S.C., Cary, G.J., Smith, A.L., Davies, I.D., Driscoll, D.A., Gill, A.M., Peakall, R., 2013. How does ecological disturbance influence genetic diversity? Trends Ecol. Evol. 28 (11), 670–679.

Bechtold, W.A., Patterson, P.L., 2005. The Enhanced Forest Inventory and Analysis Program–National Sampling Design and Estimation Procedures. USDA Forest Service, Southern Research Station.

Belgiu, M., Drăguţ, L., 2016. Random forest in remote sensing: A review of applications and future directions. ISPRS J. Photogramm. Remote Sens. 114, 24–31.

Birdsey, R.A., Lewis, G.M., 2002. Current and historical trends in use, management, and disturbance of US forestlands. In: The Potential of US Forest Soils to Sequester Carbon and Mitigate the Greenhouse Effect. CRC Press, New York, pp. 15–34.

Bouvet, A., Mermoz, S., Ballère, M., Koleck, T., Le Toan, T., 2018. Use of the SAR shadowing effect for deforestation detection with Sentinel-1 time series. Remote Sens. 10 (8), 1250.

Bradford, J.B., Weishampel, P., Smith, M.-L., Kolka, R., Birdsey, R.A., Ollinger, S.V., Ryan, M.G., 2010. Carbon pools and fluxes in small temperate forest landscapes: variability and implications for sampling design. For. Ecol. Manag. 259 (7), 1245–1254.

Brand, G.J., Nelson, M.D., Wendt, D.G., Nimerfro, K.K., 2000. The hexagon/panel system for selecting FIA plots under an annual inventory. In: McRoberts, Ronald E., Reams, Gregory A., Van Deusen, Paul C. (Eds.), Proceedings of the First Annual Forest Inventory and Analysis Symposium; Gen. Tech. Rep. NC-213. St. Paul, MN: US Department of Agriculture, Forest Service, North Central Research Station: 8-13.

Breiman, L., 2001. Random forests. Mach. Learn. 45 (1), 5–32. https://doi.org/10.1023/A:1010933404324.

Buma, B., Schultz, C., 2020. Disturbances as opportunities: learning from disturbance-response parallels in social and ecological systems to better adapt to climate change. J. Appl. Ecol. 57 (6), 1113–1123.

Chambers, J.Q., Fisher, J.I., Zeng, H., Chapman, E.L., Baker, D.B., Hurtt, G.C., 2007. Hurricane Katrina's carbon footprint on US Gulf Coast forests. Science 318 (5853), 1107.

Cohen, W.B., Goward, S.N., 2004. Landsat's role in ecological applications of remote sensing. Bioscience 54 (6), 535–545.

DeVries, B., Verbesselt, J., Kooistra, L., Herold, M., 2015. Robust monitoring of small-scale forest disturbances in a tropical montane forest using Landsat time series. Remote Sens. Environ. 161, 107–121. https://doi.org/10.1016/j.rse.2015.02.012.

Dubayah, R., Blair, J.B., Goetz, S., Fatoyinbo, L., Hansen, M., Healey, S., Luthcke, S., 2020. The global ecosystem dynamics investigation: high-resolution laser ranging of the Earth's forests and topography. Sci. Remote Sens. 1, 100002.

Egnell, G., 2017. A review of Nordic trials studying effects of biomass harvest intensity on subsequent forest production. For. Ecol. Manag. 383, 27–36.

EPA, 2006. Level III Ecoregions of North America. Retrieved from. https://gaftp.epa.gov/EPADataCommons/ORD/Ecoregions/cec_na/NA_LEVEL_III.pdf.

FIA Field Guide, 2019. National Core Field Guide version 9.1. Retrieved from. https://www.fia.fs.fed.us/library/field-guides-methods-proc/.

Frazer, G.W., Magnussen, S., Wulder, M.A., Niemann, K.O., 2011. Simulated impact of sample plot size and co-registration error on the accuracy and uncertainty of LiDAR-derived estimates of forest stand biomass. Remote Sens. Environ. 115 (2), 636–649. https://doi.org/10.1016/j.rse.2010.10.008.

Fridman, J., Holm, S., Nilsson, M., Nilsson, P., Ringvall, A.H., Ståhl, G., 2014. Adapting National Forest Inventories to changing requirements–the case of the Swedish National Forest Inventory at the turn of the 20th century. Silva Fennica 48 (3), 1–29.

Gelfand, A.E., Ghosh, S., Clark, J.S., 2013. Scaling integral projection models for analyzing size demography. Stat. Sci. 28 (4), 641–658.

Gillespie, A.J.R., 1999. Rationale for a national annual forest inventory program. J. For. 97 (12), 16–20.

Hansen, M.C., Loveland, T.R., 2012. A review of large area monitoring of land cover change using Landsat data. Remote Sens. Environ. 122, 66–74.

Hansen, M.C., Potapov, P.V., Moore, R., Hancher, M., Turubanova, S.A., Tyukavina, A., Townshend, J.R.G., 2013. High-resolution global maps of 21st-century forest cover change. Science (New York, N.Y.) 342 (2013), 850–853. https://doi.org/10.1126/science.1244693.

Hanson, J.J., Lorimer, C.G., 2007. Forest structure and light regimes following moderate wind storms: implications for multi-cohort management. Ecol. Appl. 17 (5), 1325–1340.

Harris, R.M.B., Beaumont, L.J., Vance, T.R., Tozer, C.R., Remenyi, T.A., Perkins-Kirkpatrick, S.E., Andrew, N.R., 2018. Biological responses to the press and pulse of climate trends and extreme events. Nat. Clim. Chang. 8 (7), 579–587.

He, L., Chen, J.M., Zhang, S., Gomez, G., Pan, Y., McCullough, K., Masek, J.G., 2011. Normalized algorithm for mapping and dating forest disturbances and regrowth for the United States. Int. J. Appl. Earth Obs. Geoinf. 13 (2), 236–245.

Healey, S.P., Yang, Z., Cohen, W.B., Pierce, D.J., 2006. Application of two regression-based methods to estimate the effects of partial harvest on forest structure using Landsat data. Remote Sens. Environ. 101 (1), 115–126. https://doi.org/10.1016/J.RSE.2005.12.006.

Hermosilla, T., Wulder, M.A., White, J.C., Coops, N.C., Hobart, G.W., 2015. An integrated Landsat time series protocol for change detection and generation of annual gap-free surface reflectance composites. Remote Sens. Environ. 158, 220–234. https://doi.org/10.1016/j.rse.2014.11.005.

Hill, T.C., Ryan, C.M., Williams, M., 2015. A framework for estimating forest disturbance intensity from successive remotely sensed biomass maps: moving beyond average biomass loss estimates. Carbon Balance Manag. 10 (1), 27. https://doi.org/10.1186/s13021-015-0039-0.

Hirschmugl, M., Deutscher, J., Sobe, C., Bouvet, A., Mermoz, S., Schardt, M., 2020. Use of SAR and optical time series for tropical forest disturbance mapping. Remote Sens. 12 (4), 727.

Homer, C., Dewitz, J., Jin, S., Xian, G., Costello, C., Danielson, P., Stehman, S., 2020. Conterminous United States land cover change patterns 2001–2016 from the 2016 national land cover database. ISPRS J. Photogramm. Remote Sens. 162, 184–199.

Hoppus, M., Riemann, R., Lister, A., 2000. Remote sensing strategies for Forest inventory and analysis utilizing the FIA plot database. In: *8th Forest Service Biennial Remote Sensing Applications Conference*. Albuquerque, NM.

Huang, C., Goward, S.N., Masek, J.G., Gao, F., Vermote, E.F., Thomas, N., Townshend, J.R.G., 2009. Development of time series stacks of landsat images for reconstructing forest disturbance history. Int. J. Digital Earth 2 (3), 195–218. https://doi.org/10.1080/17538940902801614.

Huang, C., Goward, S.N., Masek, J.G., Thomas, N., Zhu, Z., Vogelmann, J.E., 2010a. An automated approach for reconstructing recent forest disturbance history using dense Landsat time series stacks. Remote Sens. Environ. 114 (1), 183–198. https://doi.org/10.1016/j.rse.2009.08.017.

Huang, C., Thomas, N., Goward, S.N., Masek, J.G., Zhu, Z., Townshend, J.R.G., Vogelmann, J.E., 2010b. Automated masking of cloud and cloud shadow for forest change analysis using Landsat images. Int. J. Remote Sens. 31 (20), 5449–5464.

Huang, C., Ling, P.-Y., Zhu, Z., 2015. North Carolina's forest disturbance and timber production assessed using time series Landsat observations. Int. J. Digital Earth 8 (12), 947–969.

Hurtt, G.C., Chini, L.P., Frolking, S., Betts, R.A., Feddema, J., Fischer, G., Janetos, A., 2011. Harmonization of land-use scenarios for the period 1500–2100: 600 years of global gridded annual land-use transitions, wood harvest, and resulting secondary lands. Clim. Chang. 109 (1–2), 117.

Ju, J., Roy, D.P., 2008. The availability of cloud-free Landsat ETM+ data over the conterminous United States and globally. Remote Sens. Environ. 112 (3), 1196–1211.

Kennedy, R.E., Yang, Z., Cohen, W.B., 2010. Detecting trends in forest disturbance and recovery using yearly Landsat time series: 1. LandTrendr - temporal segmentation algorithms. Remote Sens. Environ. 114 (12), 2897–2910. https://doi.org/10.1016/j.rse.2010.07.008.

Lefsky, M.A., Cohen, W.B., Parker, G.G., Harding, D.J., 2002. Lidar remote sensing for ecosystem studies: Lidar, an emerging remote sensing technology that directly measures the three-dimensional distribution of plant canopies, can accurately estimate vegetation structural attributes and should be of particular inte. BioScience 52 (1), 19–30.

Legaard, K.R., Sader, S.A., Simons-Legaard, E.M., 2015. Evaluating the impact of abrupt changes in forest policy and management practices on landscape dynamics: analysis of a Landsat image time series in the Atlantic northern Forest. PLoS One 10 (6), e0130428.

Leverkus, A.B., Lindenmayer, D.B., Thorn, S., Gustafsson, L., 2018. Salvage logging in the world's forests: interactions between natural disturbance and logging need recognition. Glob. Ecol. Biogeogr. 27 (10), 1140–1154. https://doi.org/10.1111/geb.12772.

Lindenmayer, D.B., Burton, P.J., Franklin, J.F., 2008. Salvage Logging and its Ecological Consequences. Island Press, Washington DC.

Ling, P.-Y., Baiocchi, G., Huang, C., 2016. Estimating annual influx of carbon to harvested wood products linked to forest management activities using remote sensing. Clim. Chang. 134 (1–2), 45–58.

Lu, D., Chen, Q., Wang, G., Liu, L., Li, G., Moran, E., 2016. A survey of remote sensing-based aboveground biomass estimation methods in forest ecosystems. Int. J. Digital Earth 9 (1), 63–105. https://doi.org/10.1080/17538947.2014.990526.

Masek, J.G., Vermote, E.F., Saleous, N.E., Wolfe, R., Hall, F.G., Huemmrich, K.F., Lim, T.-K., 2006. A Landsat surface reflectance dataset for North America, 1990-2000. IEEE Geosci. Remote Sens. Lett. 3 (1), 68–72.

Matasci, G., Hermosilla, T., Wulder, M.A., White, J.C., Coops, N.C., Hobart, G.W., Zald, H.S.J., 2018. Large-area mapping of Canadian boreal forest cover, height, biomass and other structural attributes using Landsat composites and lidar plots. Remote Sens. Environ. 209 (June 2017), 90–106. https://doi.org/10.1016/j.rse.2017.12.020.

McRoberts, R.E., Tomppo, E.O., 2007. Remote sensing support for national forest inventories. Remote Sens. Environ. 110 (4), 412–419.

McRoberts, R.E., Bechtold, W.A., Patterson, P.L., Scott, C.T., Reams, G.A., 2005. The enhanced Forest inventory and analysis program of the USDA Forest Service: historical perspective and announcement of statistical documentation. J. For. 103 (6), 304–308.

McRoberts, R.E., Cohen, W.B., Naesset, E., Stehman, S.V., Tomppo, E.O., 2010. Using remotely sensed data to construct and assess forest attribute maps and related spatial products. Scand. J. For. Res. 25 (4), 340–367.

Meigs, G.W., Kennedy, R.E., Gray, A.N., Gregory, M.J., 2015. Spatiotemporal dynamics of recent mountain pine beetle and western spruce budworm outbreaks across the Pacific Northwest Region, USA. For. Ecol. Manag. 339, 71–86.

Mikoláš, M., Svitok, M., Tejkal, M., Leitão, P.J., Morrissey, R.C., Svoboda, M., Fontaine, J.B., 2015. Evaluating forest management intensity on an umbrella species: Capercaillie persistence in Central Europe. For. Ecol. Manag. 354, 26–34.

Mushinski, R.M., Gentry, T.J., Dorosky, R.J., Boutton, T.W., 2017. Forest harvest intensity and soil depth alter inorganic nitrogen pool sizes and ammonia oxidizer community composition. Soil Biol. Biochem. 112, 216–227.

Nelson, M.D., Healey, S.P., Moser, W.K., Hansen, M.H., 2009. Combining satellite imagery with forest inventory data to assess damage severity following a major blowdown event in northern Minnesota, USA. Int. J. Remote Sens. 30 (19), 5089–5108.

Neuenschwander, A., Pitts, K., 2019. The ATL08 land and vegetation product for the ICESat-2 Mission. Remote Sens. Environ. 221, 247–259.

Olofsson, P., Foody, G.M., Herold, M., Stehman, S.V., Woodcock, C.E., Wulder, M.A., 2014. Good practices for estimating area and assessing accuracy of land change. Remote Sens. Environ. 148, 42–57.

Olsson, B.A., Bengtsson, J., Lundkvist, H., 1996. Effects of different forest harvest intensities on the pools of exchangeable cations in coniferous forest soils. For. Ecol. Manag. 84 (1–3), 135–147.

Omernik, J.M., 1987. Ecoregions of the conterminous United States. Ann. Assoc. Am. Geogr. 77 (1), 118–125. https://doi.org/10.1111/j.1467-8306.1987.tb00149.x.

Omernik, J.M., 2004. Perspectives on the nature and definition of ecological regions. Environ. Manag. https://doi.org/10.1007/s00267-003-5197-2.

Pal, M., 2005. Random forest classifier for remote sensing classification. Int. J. Remote Sens. 26 (1), 217–222.

Panfil, S.N., Gullison, R.E., 1998. Short term impacts of experimental timber harvest intensity on forest structure and composition in the Chimanes Forest, Bolivia. For. Ecol. Manag. 102 (2–3), 235–243.

Parrotta, J.A., Francis, J.K., Knowles, O.H., 2002. Harvesting intensity affects forest structure and composition in an upland Amazonian forest. For. Ecol. Manag. 169 (3), 243–255.

Pickett, S.T.A., White, P.S., 2013. The Ecology of Natural Disturbance and Patch Dynamics. Elsevier.

Potapov, P., Li, X., Hernandez-Serna, A., Tyukavina, A., Hansen, M.C., Kommareddy, A., Silva, C.E., 2021. Mapping global forest canopy height through integration of GEDI and Landsat data. Remote Sens. Environ. 253, 112165.

Reid, D.J., Quinn, J.M., Wright-Stow, A.E., 2010. Responses of stream macroinvertebrate communities to progressive forest harvesting: influences of harvest intensity, stream size and riparian buffers. For. Ecol. Manag. 260 (10), 1804–1815.

Rosen, P.A., Hensley, S., Shaffer, S., Veilleux, L., Chakraborty, M., Misra, T., Satish, R., 2015. The NASA-ISRO SAR mission-An international space partnership for science and societal benefit. In: 2015 IEEE Radar Conference (RadarCon). IEEE, pp. 1610–1613.

Rüetschi, M., Small, D., Waser, L.T., 2019. Rapid detection of windthrows using Sentinel-1 C-band SAR data. Remote Sens. 11 (2), 115.

Scheller, R.M., Hua, D., Bolstad, P.V., Birdsey, R.A., Mladenoff, D.J., 2011. The effects of forest harvest intensity in combination with wind disturbance on carbon dynamics in Lake states Mesic forests. Ecol. Model. 222 (1), 144–153.

Schleeweis, K.G., Goward, S.N., Huang, C., Dwyer, J.L., Dungan, J.L., Lindsey, M.A., Masek, J.G., 2016. Selection and quality assessment of Landsat data for the north American forest dynamics forest history maps of the US. Int. J. Digital Earth 9 (10), 963–980.

Schleeweis, K.G., Moisen, G.G., Schroeder, T.A., Toney, C., Freeman, E.A., Goward, S.N., Dungan, J.L., 2020. US National Maps Attributing Forest Change: 1986–2010. Forests 11 (6), 653.

Seidl, R., Thom, D., Kautz, M., Martin-Benito, D., Peltoniemi, M., Vacchiano, G., Reyer, C.P.O., 2017, June 1. Forest disturbances under climate change. *Nature Climate Change*. Nature Publishing Group. https://doi.org/10.1038/nclimate3303.

Senf, C., Seidl, R., 2021. Mapping the forest disturbance regimes of Europe. Nat. Sustain. 4 (1), 63–70.
Sheffield, R.M., Thompson, M.T., 1992. Hurricane Hugo: Effects on South Carolina's Forest Resource, Vol. 284. USDA Forest Service, Southeastern Forest Experiment Station Research Paper.
Sieg, C.H., Linn, R.R., Pimont, F., Hoffman, C.M., McMillin, J.D., Winterkamp, J., Baggett, L.S., 2017. Fires following bark beetles: factors controlling severity and disturbance interactions in ponderosa pine. Fire Ecol. 13 (3), 1–23. https://doi.org/10.4996/fireecology.130300123.
Singleton, M.P., Thode, A.E., Meador, A.J.S., Iniguez, J.M., 2019. Increasing trends in high-severity fire in the southwestern USA from 1984 to 2015. For. Ecol. Manag. 433, 709–719.
Siry, J.P., 2002. Intensive timber management practices. Southern Forest Resource Assess. 14, 327–340.
Smith, W.B., 2002. Forest inventory and analysis: a national inventory and monitoring program. Environ. Pollut. 116, S233–S242.
Smith, W.B., Darr, D.R., 2004. US Forest Resource Facts and Historical Trends.
Soutiere, E.C., 1979. Effects of timber harvesting on marten in Maine. J. Wildl. Manag. 850–860.
Stehman, S.V., Czaplewski, R.L., 1998. Design and analysis for thematic map accuracy assessment: fundamental principles. Remote Sens. Environ. 64 (3), 331–344.
Storey, J., Choate, M., Lee, K., 2014. Landsat 8 operational land imager on-orbit geometric calibration and performance. Remote Sens. 6 (11), 11127–11152.
Storey, J., Roy, D.P., Masek, J., Gascon, F., Dwyer, J., Choate, M., 2016. A note on the temporary misregistration of Landsat-8 operational land imager (OLI) and Sentinel-2 multi spectral instrument (MSI) imagery. Remote Sens. Environ. 186, 121–122.
Sugarbaker, L., Constance, E.W., Heidemann, H.K., Jason, A.L., Lucas, V., Saghy, D., Stoker, J.M., 2014. The 3D Elevation Program Initiative: a Call for Action. US Geological Survey.
Tao, X., Huang, C., Zhao, F., Schleeweis, K., Masek, J., Liang, S., 2019. Mapping forest disturbance intensity in North and South Carolina using annual Landsat observations and field inventory data. Remote Sens. Environ. 221 (November 2018), 351–362. https://doi.org/10.1016/j.rse.2018.11.029.
Thom, D., Seidl, R., 2016. Natural disturbance impacts on ecosystem services and biodiversity in temperate and boreal forests. Biol. Rev. 91 (3), 760–781. https://doi.org/10.1111/brv.12193.
Tomppo, E., Olsson, H., Ståhl, G., Nilsson, M., Hagner, O., Katila, M., 2008. Combining national forest inventory field plots and remote sensing data for forest databases. Remote Sens. Environ. 112 (5), 1982–1999.
Torres, R., Snoeij, P., Geudtner, D., Bibby, D., Davidson, M., Attema, E., Brown, M., 2012. GMES Sentinel-1 mission. Remote Sens. Environ. 120, 9–24.
Treuhaft, R.N., Law, B.E., Asner, G.P., 2004. Forest attributes from radar interferometric structure and its fusion with optical remote sensing. BioScience 54 (6), 561–571.
Turner, B.L., Clark, W.C., Kates, R.W., Richards, J.F., Matthews, J.T., Meyer, W.B., 1993. The Earth as Transformed by Human Action: Global and Regional Changes in the Biosphere over the Past 300 Years. Cambridge University Press. Retrieved from. https://books.google.com/books?id=7GI0AAAAIAAJ.
U.S. Environmental Protection Agency, 2010. Level III Ecoregions of the Continental United States (Revision of Omernik, 1987), Map.
Vitousek, P.M., Mooney, H.A., Lubchenco, J., Melillo, J.M., 1997. Human domination of Earth's ecosystems. Science 277 (5325), 494–499.
White, J.C., Wulder, M.A., Hermosilla, T., Coops, N.C., Hobart, G.W., 2017. A nationwide annual characterization of 25 years of forest disturbance and recovery for Canada using Landsat time series. Remote Sens. Environ. 194, 303–321. https://doi.org/10.1016/j.rse.2017.03.035.
Woodall, C.W., Leutscher, B., 2005. Extending and intensifying the FIA inventory of down forest fuels: boundary waters canoe area and pictured rocks National Lakeshore. In: *Proceedings of the fifth annual forest inventory and analysis symposium; 2003 November 18-20; New Orleans, LA. Gen. Tech. Rep. WO-69. Washington, DC: US Department of Agriculture Forest Service. 222p.* (Vol. 69).
Woodcock, C.E., Allen, R., Anderson, M., Belward, A., Bindschadler, R., Cohen, W., Helmer, E., 2008. Free access to Landsat imagery. Science 320 (5879), 1011.
Wulder, M.A., White, J.C., Nelson, R.F., Næsset, E., Ørka, H.O., Coops, N.C., Gobakken, T., 2012. Lidar sampling for large-area forest characterization: A review. Remote Sens. Environ. 121, 196–209.
Wulder, M.A., Loveland, T.R., Roy, D.P., Crawford, C.J., Masek, J.G., Woodcock, C.E., Cohen, W.B., 2019. Current status of Landsat program, science, and applications. Remote Sens. Environ. 225, 127–147.
Yanai, R.D., Currie, W.S., Goodale, C.L., 2003. Soil carbon dynamics after forest harvest: an ecosystem paradigm reconsidered. Ecosystems 197–212.
Zhang, C., Zhou, Y., Qiu, F., 2015. Individual tree segmentation from LiDAR point clouds for urban forest inventory. Remote Sens. 7 (6), 7892–7913.
Zhao, F., Huang, C., Goward, S.N., Schleeweis, K., Rishmawi, K., Lindsey, M.A., Michaelis, A., 2018. Development of Landsat-based annual US forest disturbance history maps (1986–2010) in support of the North American Carbon Program (NACP). Remote Sens. Environ. 209, 312–326. https://doi.org/10.1016/J.RSE.2018.02.035.
Zhu, Z., Wulder, M.A., Roy, D.P., Woodcock, C.E., Hansen, M.C., Radeloff, V.C., Scambos, T.A., 2019a. Benefits of the free and open Landsat data policy. Remote Sens. Environ. 224, 382–385. https://doi.org/10.1016/j.rse.2019.02.016.
Zhu, Z., Zhang, J., Yang, Z., Aljaddani, A.H., Cohen, W.B., Qiu, S., Zhou, C., 2019b. Continuous monitoring of land disturbance based on Landsat time series. Remote Sens. Environ. 238 (November 2018), 111116. https://doi.org/10.1016/j.rse.2019.03.009.